Development of Electrospun PAN Fibers Used as Electrodes for Flow Cell Applications

by

Muhammad Murtaza

A thesis

presented to the University Of Waterloo

in fulfillment of the

thesis requirement for the degree of

Master of Applied Science

in

Chemical Engineering

Waterloo, Ontario, Canada, 2019

Author's Declaration

I hereby declare that I am the sole author of this thesis. This is a true copy of the thesis, including any required final revisions, as accepted by my examiners.

I understand that my thesis may be made electronically available to the public.

Abstract

The increase in energy consumption coupled with global climate change have generated a keen interest in renewable energy resources in the scientific world. Grid scale energy storage solutions are required in order to bridge the mismatch between power generation and power consumption due to the intermittent nature of renewable energy resources. Redox flow batteries have shown great potential as grid scale energy storage solution due to their advantages over other technologies. However, redox flow battery technology still requires development such as the need to increase their power density and efficiency. Previously, Liu, Kok, Kim, Barton, Brushett and Gostick (2017) fabricated porous electrode layers to increase the specific surface area as they noticed poor kinetic performance of the commercial electrodes. These electrodes had better overall performance but low electrical conductivity. The objective of this thesis was achieved by improving the electrical conductivity 2.5 times of the porous electrode layer to that of Liu, Kok, Kim, Barton, Brushett and Gostick (2017), while maintaining other performance related properties such as porosity, permeability and surface area. Increasing the electrical conductivity of the porous electrode layer decreases internal resistances within the cell, which results in decreased ohmic losses in the performance curves of the flow battery and consequently higher voltage efficiency. A brief study on the mechanical properties of the porous electrode layer was also conducted to gain an insight into the integrity of the porous electrode layer.

Acknowledgements

I begin by thanking and submitting to The All Mighty Allah, who created the path, incorporated ease and guided me to the end of my master's journey. I would like to sincerely thank my supervisor, Jeff Gostick, for trusting in me and making me a part of his team. Jeff motivated, encouraged and provided his knowledge and experience at every point, to make sure things kept going and extracted maximum potential out of me. I would like to thank Shashi Yadav who trained me and got me going on the electrospinning setup, the backbone for all my research. I would like to thank Yong for helping with LabView programing and providing insight and knowledge for different hurdles faced during my research. I would also like to thank Kannika for helping with 3 point bending test.

I would also like to acknowledge my wife, Neha Khan, for her love, support, sacrifices and understanding as I completed my master's research. I would also like to thank my family, especially my loving parents for their sacrifices, their emotional and financial support to help achieve my goals.

The electrospinning setup, permeability and electrical conductivity measurement devices used for this study were designed and built by members of the PMEAL team. Graphene oxide/DMF solutions were prepared by Azam Nasr from Michael Pope's Research Lab at University of Waterloo. The 3-point bending test conducted for this

study was by Kannika Onyu on an equipment at Leonardo Simon's Research Lab at University of Waterloo.

Table of Contents

List of Figures

List of Tables

List of Abbreviations

IEA – International Energy Agency

EES – Electric Energy Storage

PAN – PolyAcryloNitrile

PHS – Pumped Hydroelectric Storage

CAES – Compressed Air Energy Storage

HS – Hydrogen Storage

PEL – Porous Electrode Layer

DMF – N, N Dimethylformamide

GO – Graphene Oxide

rGO – reduced Graphene oxide

MPRG – Michael Pope's Research Group

SEM – Scanning Electron Microscopy

MW – Molecular Weight

BET – Brunauer – Emmett Theory

DVS – Digital Vapor Sorption

List of Symbols

CO_2 – Carbon dioxide

N_2 – Nitrogen

1. Introduction

1.1. Motivation

With the continual increase of the world population and technological advancements in the developing worlds, the growth in energy demand has been relentless in the past few decades. Enerdata[1] and International Energy Agency (IEA)[2] report that the worldwide energy consumption grew by 2.3% in 2018. This growth rate in energy consumption is nearly twice that reached in 2010.[2] Furthermore, the IEA also reports that about 14% of the world's population is still living without any access to energy and not yet contributing to the growth in energy consumption.[3] The rapid technological advances has significantly increased the importance of electricity production in the past few years. Enerdata[1] and IEA[2] report that the electricity demand increased by 3.5% - 4% in 2018, which is nearly twice the energy consumption growth. Figure 1 shows the change in electricity consumption from 1990 to 2018.

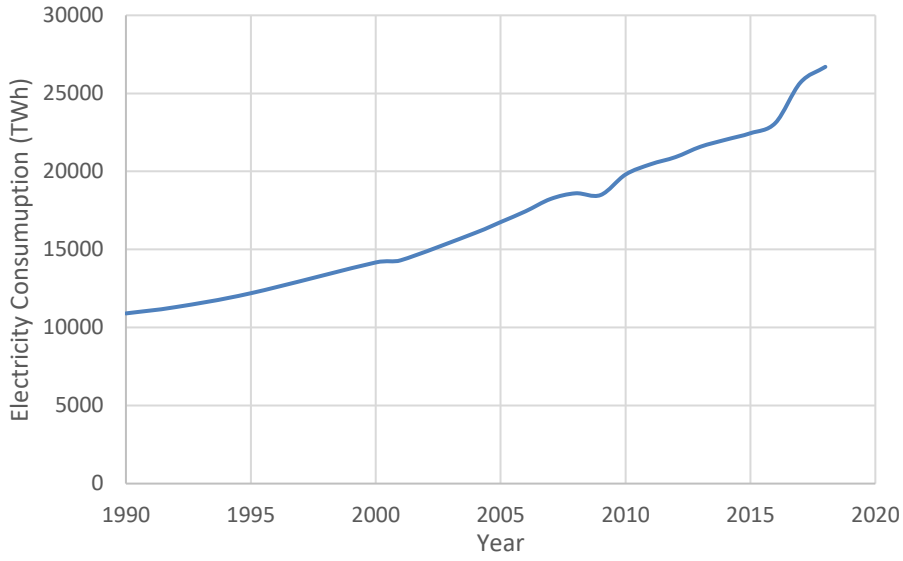

Figure 1: Global energy consumption from 1990 to 2018 based on data from Enerdata[1] and IEA[4]

Although the growth of electricity demand and consumption is inevitable, the major concern lies in how the electricity is generated. Fossil fuels or carbon-based fuels, such as oil, coal and natural gas, have been used as a source of energy for as long as we can remember. To date, fossil fuels remain the dominant source of energy generation, especially in the electricity sector. Figure 2 shows the percentage of global electricity produced using different sources in 2018.

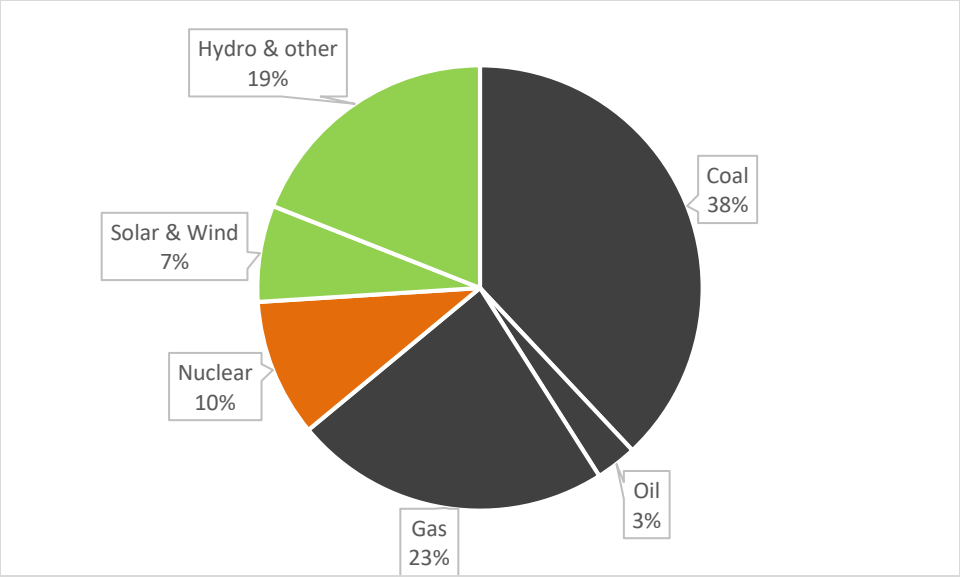

Figure 2: The breakdown of energy sources for worldwide electricity generation in 2018[2]

The continuous and excessive use of carbon-based fuels has had detrimental effects on our environment. The increased use of carbon-based fuels causes increased emissions of carbon dioxide (CO_2) into the atmosphere. Researchers at NASA believe that CO_2 is one of the main causes of climate change.[5] Consequently, renewable energy technologies have attracted significant scientific and public interest in the past few years. Renewable energy sources yield decentralized electricity production with fewer environmental hazards.[6] Renewable energy sources such as solar, hydro, geothermal, are abundant, readily accessible and viewed as the future of energy production. Although abundant, renewable energy has a major drawback of being intermittent. Renewable energy sources fluctuate independently from demand and pose a serious risk to the current power grid. The mismatch between demand and supply will cause power plant auxiliaries to fail. The power grid can be destabilized by 20% integration of renewables

into the current system.[7]

On the bright side, conversion technologies are well developed and becoming more and more affordable. For renewable energy sources to significantly contribute sustainable energy use, further development of large-scale electric energy storage (EES) device is required, which stores energy when available and supplies energy when needed.[6] These devices will improve grid stability and effective utilization of the entire grid system with renewables well integrated into them.[7], [8]

1.2. Objectives

In order to effectively integrate flow batteries at the grid scale, it is important to further improve the power density and efficiency of flow batteries. The high-level objective of this thesis is to improve the power density and efficiency of flow battery systems by enhancing the electrode systems used in flow batteries.

Based on previous work done by Liu, Kok, Kim, Barton, Brushett and Gostick (2017)[9], commercial flow battery electrodes, such as SGL25AA and Toray 90, exhibit poor kinetic performance, which has an adverse impact on the power density and efficiency. Liu, Kok, Kim, Barton, Brushett and Gostick (2017)[9] addressed the issue of kinetic performance in their research work by improving specific surface area of the porous electrode layer. Liu, Kok, Kim, Barton, Brushett and Gostick (2107)[9] fabricated homemade electrodes

with 30 times smaller fiber diameter than commercial electrodes using the electrospinning technique. Reduction of fiber diameter increased the number of fibers in a given volume and significantly raised their specific surface area. Consequently, these electrodes exhibited better overall performance than SGL25AA.

This thesis will focus on further developing electrodes, to further improve their performance. Permeability, porosity, electrical conductivity and specific surface area are a few key properties that affect the performance of an electrode.[9], [10] Liu, Kok, Kim, Barton, Brushett and Gostick (2017)[9] was able to increase the specific surface area, without adversely affecting other key properties except electrical conductivity. The thesis will report work done towards improving the electrical conductivity of electrospun polyacrylonitrile (PAN) fibers in order to increase the power density and efficiency of the flow battery. Higher electrical conductivity should reduce the ohmic losses within cell, so that more current density can be obtained from specific amount of reactant consumed. A higher current density directly increases the power density of the cell. On the other hand, as ohmic losses decrease, the voltage efficiency of the cell increases. This is illustrated in Figure 3. The performance corresponding to blue curve is significantly better and so can produce the same amount of power at low current and overpotential.

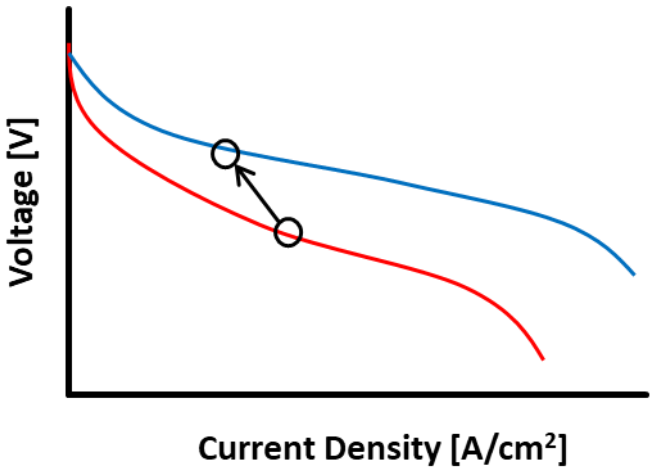

Figure 3: Polarization curves for two cells. The blue curve exhibits significantly better performance than the red curve in terms of improved conductance.

Primarily two different methods have been reported in literature to improve the electrical conductivity of electrospun PAN fibers. The first method is to increase the carbonization temperature([11], [12]), while the second method is to add additives such as carbon black, graphene and carbon nanotubes.[13] With an increase in the carbonization temperature, the carbon fibers become graphitic in nature and hence, become more electrically conductive.[11] However a short stabilization time during carbonization cycle was provided by Liu, Kok, Kim, Barton, Brushett and Gostick (2017)[9], which reduces the quality of the fibers. Higher stabilization time increases the density of the fibers[14], which especially helps with the second objective of this thesis, which will be discussed later in this section.

Although the addition of additives, such as graphene, increases the electrical conductivity, graphene particles do not well integrate into the carbon fibers. Post carbonization, the graphene particles form blobs within fibers, which can adversely affect overall performance of the electrode.[13] This thesis will study the effect of high carbonization temperature together with increased stabilization time and addition of graphene in the fibers. The additive approach will be optimized to avoid formation of blobs. Together with the two approaches, a third approach will be studied which will focus on increasing the contact area between fibers to facilitate better electron flow and study its effect on key performance parameters.

The second objective of the thesis is to study the integrity of electropsun PAN fibers. Electrospun PAN fibers are generally restricted to those applications which do not rely on their mechanical strength, as these fiber mats are brittle in nature.[13] A study of how different methods described above affect the mechanical properties of electrospun PAN fibers will be studied in the second half of the thesis.

2. Background

2.1. Overview of Large-Scale Electrical Energy Storage Systems

Apart from the growth in demand of electricity production and the related environmental concerns, the questionable reliability of the power grid has itself stimulated the development of EES solutions. In recent memory, the August 2003 blackout of North America and the September 2011 power failure were highly publicized events which affected millions of consumers and highlighted some unreliable aspects of power grid, especially dealing with failures.[8] Generators are usually available for use in the event of a failure, however, synchronous generators cannot respond rapidly enough to keep the system stable.[15] EES systems offers a viable solution to these problems. EES can generally be classified into two main categories: direct and indirect storage. Figure 4 shows how EES systems are classified and the technologies that exist in each category.

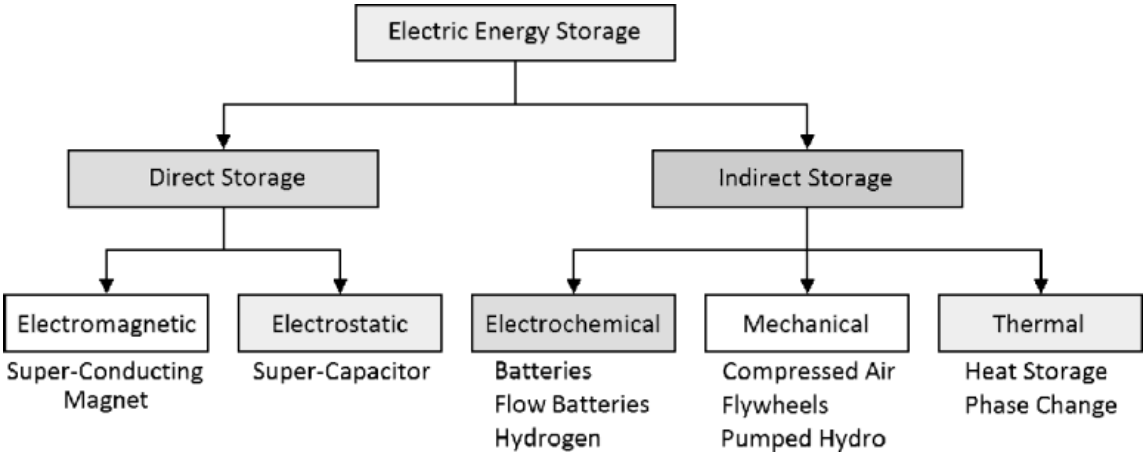

Figure 4: Classification of Electrical Energy Storage Systems and Technologies[16]

Direct EES methods store electricity in an electrostatic or electromagnetic form. Direct EES technologies consists of super conducting magnets and super – capacitors.[16] Although these devices are very efficient, they can store electricity in relatively low quantities, in the range of 50 kW – 100 kW. Furthermore, their self-discharge characteristic does not allow them to store energy for long periods.[6], [8], [16]

The only way to store electrical energy in bulk is by indirect storage methods. Technologies in this category can store electrical energy indirectly over a wide range of quantities and discharge time scales.[16]

Among the indirect EES technologies, pumped hydroelectric storage (PHS), compressed air energy storage (CAES) and lead acid batteries are relatively mature technologies. According to a survey from the Electric Power Research Institute, PHS accounts for 99%

of the global energy storage.[8], [17], [18] In PHS technology, water, stored in an upper reservoir, flows through a hydro turbine generator to generate high value electricity during peak hours. During off peak hours, the water is pumped from the lower reservoir back to the upper reservoir. This technology is mainly used for high power applications with efficiencies ranging between 65% - 80%. The major shortcoming of this technology that it requires a site with different elevations for the water reservoirs.[6], [16]–[18] Furthermore, if water is drawn from a river or lake for operational purposes, it can cause an environmental problem by endangering the aquatic life.[19]

CAES is a distant second to PHS in terms of use.[8] CAES technology has a similar concept to the PHS technology. During off – peak hours, electricity is used to compress air. The compressed air is usually stored in an underground reservoir, such as a hard rock or salt cavities, an aquifer or a depleted gas field. During peak hours, the compressed air is heated, expanded and pass through gas turbines to drive the electric generators. This technology is also used for high power applications with efficiencies of 70%. Shortcomings of this technology are access to reservoirs to store the compressed air and environmental concerns due to heating the compressed air.[16], [18]

Hydrogen storage (HS) technology is another approach which has attracted increasing interest at present times. In this technology, electrical energy is converted to hydrogen by electrolysis of water. Hydrogen is stored externally and used in fuel cells to generate

electricity, when required. The essential elements required for the technology are electrolyser units, storage facilities or tanks and fuel cell stacks. The round-trip energy efficiencies range between 20% - 50%.[17], [18], [20] The downsides of the technology are high capital cost and low round trip efficiency.[21]

Most of the mature and/or upcoming technologies have their limitations, such as site requirements, cost and efficiency. Despite current disadvantages, HS technology is developing well, but battery technology has been improving as well. Batteries as a technology are the most versatile and flexible option which overcomes most of the common concerns of the other technologies. Batteries can be easily modified, in order to increase or decrease their capacity and have efficiencies ranging between 60% - 80%.[18], [22]

Battery technology is a vast area since it comes in a wide variety of chemistries. Lead acid batteries were the earliest battery technology used early as the 1800's. This battery technology was a very cost – effective application, although it exhibits low energy and power densities and poor cycle life.[23] The disadvantages outweighed the benefits making them a weak candidate for grid storage applications. Another battery technology which has received a lot of attention is the lithium-ion battery which has high energy and power densities. However, this technology has been limited due to its safety concerns, relatively low energy density and a coupling between power and energy

storage that will be discussed further below. The lithium ion battery is also prone to thermal runaway, especially when overcharged, resulting in explosions. As a result, storage of massive scale batteries on a single site raises concerns.[24]

In conventional batteries, the electroactive materials are stored within the cell. In order to increase the energy capacity, the battery size can be increased. However, increasing the thickness of the electrode raises the resistances in the cell to mass and electron transfer, resulting in higher voltage drop and power loss within the cell.[25] This leads to a trade-off between high power density and high energy capacity of conventional batteries. Moreover, since the electrode acts as both the active material for energy storage and the electrochemical reactor for power conversion. Improving one of these aspects requires enhancement of the other.

Flow batteries provide a viable solution to these problems. A flow battery can operate with high input and output power, decoupled energy and power and its scalability gives it engineering merits over other battery technologies.[26] In flow batteries, the electroactive materials are stored externally in liquid electrolyte contained in tanks. Thermal management of battery becomes an easier task with electroactive material stored externally. The energy and power of a flow battery are decoupled since the energy capacity of the battery can be raised by increasing the volume of electrolyte, while the power density can be increased by raising the cells in a stack.[27] Table 1

provides a brief comparison of a few battery technologies.

Table 1: Comparison of different battery technologies[28], [29]

Battery Technology	Power Rating (MW)	Discharge duration (h)	Response Time	Efficiency	Cycle life at 80% depth of discharge
Lead acid battery	kW to 10's MWs	0.1 – 4	Fast	70 – 76%	200 – 1500
Sodium Sulphur battery	0.1 – 100's MW	1 – 10	Fast	85 – 90%	210 – 4500
Lithium ion Battery	kW to 100's MWs	0.1 – 1	Fast	>90%	5000 – 7000
Flow Battery	kW to 100's MWs	1 - 20	High	75 – 85%	5000 - 14000

2.1.1. History and Classification of Flow Batteries

Flow batteries have emerged as prime contenders in development of large-scale energy storage system. The earliest flow battery was prototyped by researchers at NASA in the 1970's. The early prototype had technical limitations which halted further development until the all vanadium redox flow battery was pioneered at the University of New South Wales, Australia in the 1980's. Since then, extensive research and development has been done on flow batteries and new chemistries have been explored. Looking into their commercial status, more than 30 large scale flow battery installation companies are operational in China, Japan, United States and Europe. These installations have demonstrated the technical benefits of this technology for both off-grid and grid connected applications.[30], [31]

Flow batteries are generally classified into two main categories: conventional and hybrid flow batteries. Hybrid flow batteries are flow battery systems in which one or more

electroactive specie/component is stored internally in the battery. This class of flow battery include chemistries such as zinc-bromine and zinc-chlorine. The energy capacity of these batteries is limited to the amount of electroactive specie that can be stored internally in the cell. [27], [29]

Conventional flow batteries are flow battery systems in which electroactive materials are stored externally and introduced into the flow battery device only during operation. Conventional flow batteries include chemistries such as all vanadium, iron-chromium and bromine-polysulfide.[32] Typically, the electroactive components are dissolved in liquid electrolyte and stored in two separate external tanks, one for the negative electrode reaction and the other for the positive electrode reaction.[27] As the thesis focuses primarily on development of conventional flow batteries, a more detailed description will be provided for the conventional flow battery in this section. Figure 5 shows a schematic of a conventional flow battery.

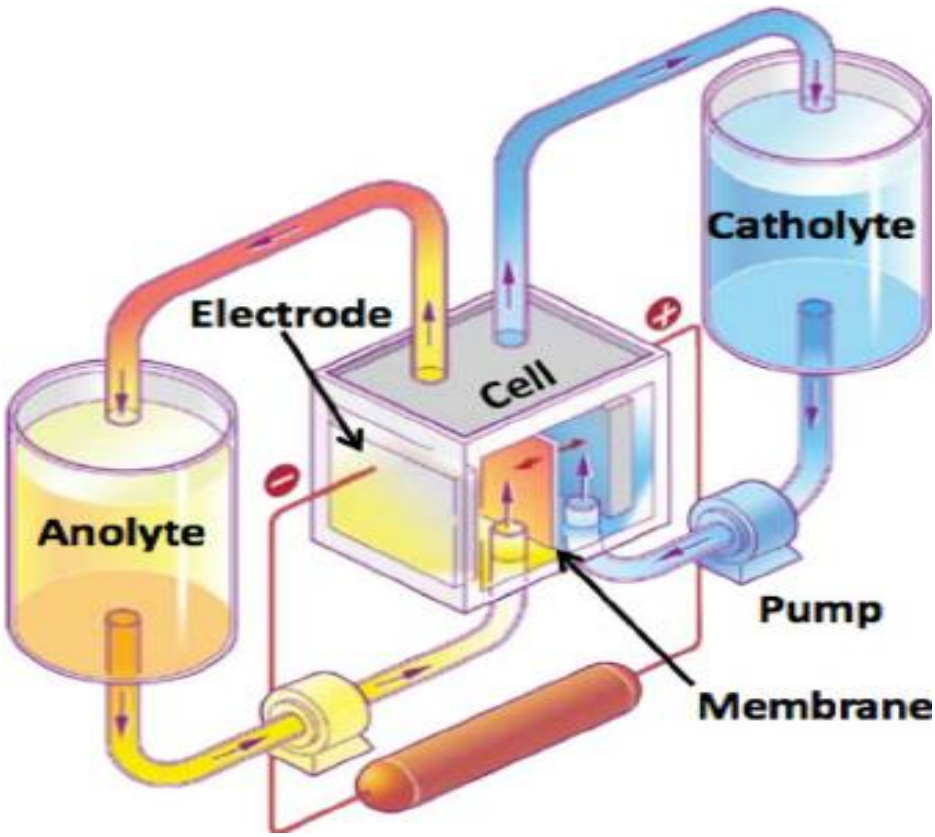

Figure 5: Schematic of conventional flow battery[33]

Flow battery performance is tied to many crucial factors. Composition of the electrolyte is the critical starting point. A flow battery electrolyte typically consists of three components: solvent, supporting electrolyte and active species. Multiple flow battery chemistries are further differentiated by the composition of the electrolyte used for operation. The electrolyte consists of components that undergo oxidation and reduction reactions, changing the oxidation states of molecules. These changes in oxidation involve electron transfer, which are forced through the external circuit of the flow battery. In order to balance electrons and completing the circuit, ions flow through the ion

exchange membrane inside the cell. Ideally, the ion exchange membrane also prevents the electrolytes of the positive and the negative electrodes from mixing.

Flow batteries are composed of two half – cells, into which the respective electrolytes flow, that consists of active species or redox couples. Each redox couple undergoes reversible redox reactions. The redox couple has a large influence on the performance of a flow battery as it defines the open circuit voltage of the flow battery, electrochemical reaction kinetics, the number of electrons produced per redox reaction, chemical stability of the electrolytes and the harshness of the environment to which the battery components are exposed.[33]

Electrode assembly is a core component of a flow battery as it provides the active sites for the redox reaction. The electrode assembly consists of two main parts: the bipolar plate and porous electrode layer. The primary function of the bipolar plate is to provide mechanical strength and support the porous electrode layer, uniformly distribute reactants within the cell, facilitate thermal management and act as current collector for the cell. [34] The energy efficiency of a flow battery is mainly governed by the activation and concentration polarization, which is determined by the porous electrode layer of the flow battery. The porous electrode layer (PEL) has four essential requirements: 1) provide active site for redox reactions; 2) electrode must be stable in harsh environments as the electrolytes can be highly acidic in nature; 3) electrode must be

electrochemically stable during operation; 4) electrode must have excellent electrical conductivity for fast charge transfer.[35]

Carbon and graphite material have been almost exclusively used for porous electrode layers. Carbon and graphite are known to have high electrical conductivity, excellent stability in harsh environments and a wide operating potential window, making them the best candidates for flow battery applications. Initial work focused on the fabrication of carbon materials from rayon and polyacrylonitrile (PAN). Further research into the two materials established PAN based carbon to be more favorable, as materials fabricated from PAN obtained had better properties such as higher specific surface area and more favorable microstructures. PEL's have been fabricated in many ways. The first material evaluated was the carbon cloth in 1987. However, the material did not grab much attention as it degraded mechanically during charging.[35]

The next attempt was to use a carbon-polymer composite electrode. This approach used a polymer as binder to hold the carbon particles together. It was found that the choice of the binder material significantly affected the electrical conductivity of the electrode. Future studies proposed using carbon black and graphite powder composite electrodes which produced promising results.[35]

The third approach in PEL fabrication was to make PAN based carbon or graphite fibers.

A PAN based fiber network, first developed in the 1950's, exhibited excellent electrical conductivity, surface area and stability in chemical and electrochemical environments. A lot of work has been done over the years to further enhance the properties of the PAN fibers, which include surface treatments and thermal treatment. Attempts have been made to add additives such as graphene to the fibers but still many obstacle and challenges exist. Further research is needed to deal with practical and operating aspects in particular.[35]

2.2. Porous Electrode Layer

With the focus of the thesis on developing the PEL for flow battery applications, this section will discuss key PEL characteristics which are important in determining the performance of the cell. The PEL represents both, the porous media through which the fluid flows and the surface where redox reactions take place in a flow battery. Key characteristics are briefly described below:

1) Porosity: Porosity is the percentage of the total volume that is empty (i.e. pore volume per unit of electrode volume). This is an important characteristic as it affects virtually every mass transport property of the PEL, including the effective diffusivity of the reactants through the PEL.[36] Flow battery applications require PEL with very high porosities (>75%).[37] High porosities ensure that sufficient flow of reactants and mass transfer does not limit the power density of the flow

battery.

2) Pore size: Pore size is a characteristic which influences how easily fluid can flow through the pore space. Very small pores tend to hinder flow of electrolyte through the PEL. It is possible to force a higher flowrate through the PEL, but that adds to the operational cost which is not desirable.[10]
3) Permeability: Permeability is a characteristic that affects the pressure driven transport properties of gas and liquid flowing through the PEL. Low permeability makes it difficult for reactants to reach the active sites and undergo electrochemical reactions.[38] As electrodes are typically compressed in flow cell designs, the permeability of an PEL is of utmost importance especially when compressed.
4) Specific surface area: Specific surface area is a measure of the number of active sites per unit volume. Higher surface area facilitates the redox reactions, which consequently increases the power density. However, a trade-off exists between the specific surface area and the permeability in order to achieve optimal performance of the PEL.[9]

2.3. Electrospinning

Electrospinning is a technique which has gained popularity in the industrial and scientific field over the last 20 – 30 years. Electrospinning technique is a safe and easy method to fabricate fibrous scaffolds with very high porosities, large surface area – volume ratio and nano- to micron- sized fiber diameters. The electrospinning technique has

successfully been applied for nano catalysis, protective clothing, tissue engineering, biomedical, filtration media, pharmaceutical, optical, electronics, environmental engineering and healthcare applications.[39]–[41]

An electrospinning setup consists of a high voltage power supply, polymer solution, needle, collector, syringe pump and a syringe. Figure 6 shows a schematic of an electrospinning setup. In the electrospinning process, a polymer solution is pumped at a constant rate through a needle tip. The polymer solution is held at the needle tip by its surface tension. A collector is electrically grounded and placed at a fixed distance from the needle tip. As a high voltage electric field is applied between the needle tip and the collector, the electrostatic forces caused by the accumulation of charges within the droplet overcome the surface tension forces and the hemispherical surface of the solution at the needle tip elongates to form a conical shape, also known as Taylor cone. The electrically charged jet undergoes a bending instability, causing the jet to rapidly move in multiple expanding loops, as the jet travels to the collector. As the jet extends towards the collector, in ever expanding loops, it causes solvent evaporation and stretching and thinning of polymer into nanometer diameter fibers.[41], [42]

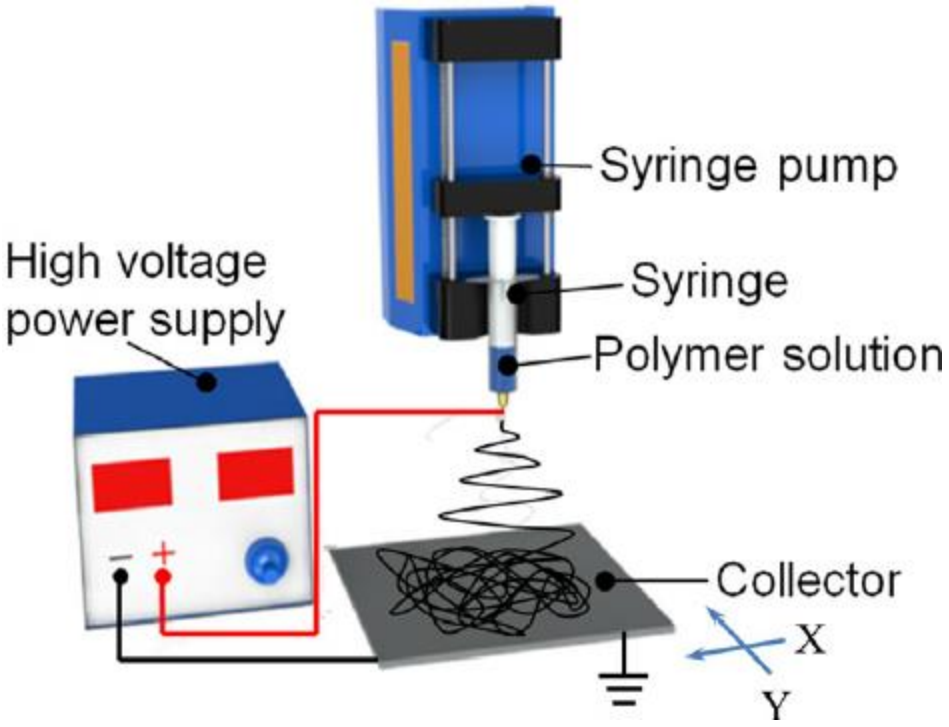

Figure 6: Electrospinning set-up schematic[43]

The electrospinning process is quite sensitive to the various combination of parameters, which can produce fibrous sheet with different fiber morphology. Some of these parameters are the polymer solution concentration, viscosity, conductivity and surface tension, temperature, humidity, wind velocity, distance between collector and needle tip, needle size and voltage applied to the generate the electric field.[42] Table 2 summarizes a few of these parameters and how they affect the electrospinning process.

Table 2: Effect of parameters on electrospinning[10], [41], [42], [44]

Parameter	Effect on fiber morphology
Solution Concentration	Low polymer concentration leads to bead formation in the fiber matrix. Too low concentration can lead to electrospraying instead of electrospinning. Fiber diameter increases with polymer concentration of the solution. Too high polymer concentration hinders continuous electrospinning, as the solution is unable to flow with ease.
Solution conductivity	High conductivity of polymer solution produces defect free fibers and smaller diameter fibers.
Voltage	Increasing applied voltage encourages bead formation and decreases fiber diameter.
Flowrate	Increased flowrate favours bead formation and fiber wetness.
Collector-needle distance	If the distance is too short, the solvent will not have enough time to vaporize. Too long distance can lead to a bead fiber mix. Increasing the distance, thins the fiber diameter.
Polymer molecular weight	Increasing the polymer molecular weight, increases the fiber diameter and inhibits bead formation.
Temperature	Increasing the temperature thins the fiber diameter.
Humidity	Increased humidity leads to pore formation on the fiber surface.

In this thesis, the polymer solution used for electrospinning consists of PAN as polymer and DMF as solvent. PAN was selected as the polymer as it obtains the highest carbon yield after carbonization of all common polymers[45], while DMF was used as it is a PAN – soluble, cheap and highly volatile solvent.[46]

2.4. Stabilization and Carbonization

The electrospun mats fabricated using PAN/DMF solution must be carbonized to make them electronically conductive for use as electrodes in flow batteries. The carbonization process consists of two main steps; stabilization and carbonization.

Stabilization is an oxidation reaction which changes nitrile groups on the polymer chain

into amide groups, which initiate dehydrogenation and cyclization reactions. Stabilization reactions transform the molecular chain into thermosetting ladder polymer.[47]–[49] Stabilization reaction takes place in an oxidizing medium, typically air. Only a few approaches have been followed to conduct the stabilization process. One approach is isothermal stabilization, which was the first method to produce continuous carbon fibers. The other approach is stepwise increase in stabilization temperature. In all of these cases, the stabilization temperature ranges between 250 – 290 °C. Figure 7 illustrates the stabilization reaction mechanism. The by-products formed during stabilization are water, carbon dioxide and HCN.[47], [50] It is crucial that enough time is given for the completeness of stabilization reactions since this affects the electrode properties drastically, especially the mechanical properties.[51]

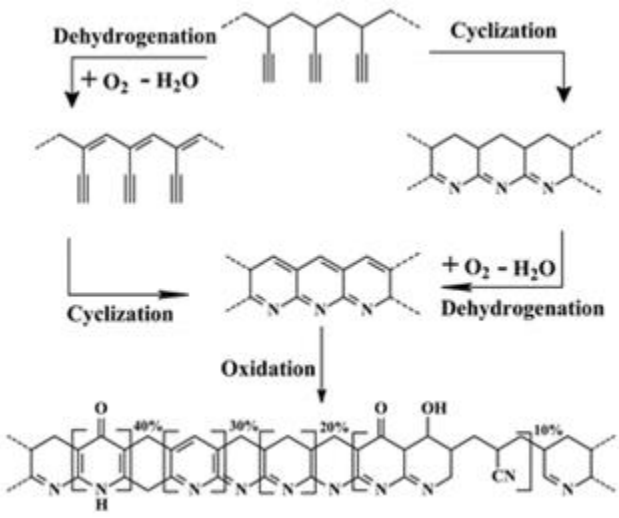

Figure 7: Reaction mechanism for stabilization reaction of PAN fibers in an oxidizing environment[52]

The next step in this process is carbonization. Carbonization is a reaction in which nitrogen and oxygen are split off the cyclic polymer chains and planar polyaromatics are formed, as shown in Figure 8. Carbonization is carried out in an inert atmosphere (eg: N_2) over temperature range 1000 – 1600 °C. During carbonization process, heterocyclic.[47] By – products formed during carbonization reaction include water, ammonia, carbon dioxide, HCN and nitrogen.[47]

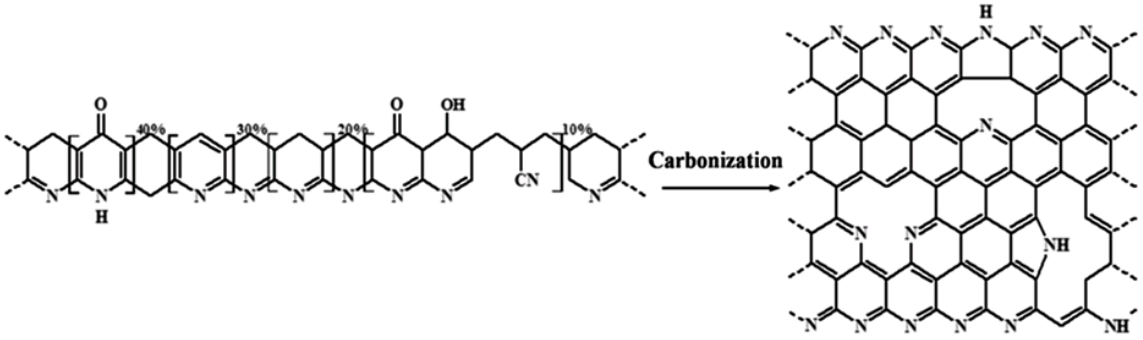

Figure 8: Reaction mechanism during carbonization of PAN fibers in an inert atmosphere[52]

Carbonization increases the density of the fibers as the fibers become more graphitic in nature. Since densification of the fibers Improves their mechanical properties, a higher carbonization temperature yields stronger carbon fibers.[53] Additionally, the extent of graphitization plays an important role in the electrical conductivity of the PEL.

3. Experimental Techniques

3.1. Chemicals

The chemicals used for experimentation were polyacrylonitrile (PAN) (average molecular weight 150,000) and N, N-dimethylformamide (DMF) (≥99.8% purity) purchased from Sigma Aldrich and single layer graphene oxide (GO) powder purchased from ACS Materials.

3.2. Preparation of PAN/DMF solution

PAN was dissolved in DMF overnight to prepare a 10 wt% solution for electrospinning. Fibrous mats prepared using 10 wt% PAN/DMF solutions were used as base materials in all the approaches to improve electrical conductivity and investigate their impact on mechanical properties. This concentration was chosen to replicate previous work done by Liu, Kok, Kim, Barton, Brushett and Gostick (2017)[9] to produce fibers in the range of 500 nm diameter.

3.3. Preparation of PAN/GO/DMF solution

PAN/GO/DMF solutions were prepared using three methods. In the first method, GO powder was added to a prepared PAN/DMF solution. The mixture was stirred overnight and then sonicated for 2 hours the next day. In the second method GO/DMF mixture was

sonicated for two hours and then mixed into a PAN/DMF solution. The solutions produced using these two methods could not be electrospun or the resultant carbonized mats contained large pieces of reduced GO (rGO) flakes that were excluded from the fibers due to a size mismatch. Such large rGO particles created blobs between fibers after carbonization which negatively affected key parameters such as permeability and porosity. Additionally, it was also observed that a sonicated mixture could not be electrospun. Sawawi, Nisbet and Simon (2013)[54] reported that sonication causes PAN chains to break in a PAN/DMF solution, which can be a possible cause for the observed effect.

The third method involved producing solutions in which GO will be dissolved in DMF solution. GO was synthesized by MPRG using the modified hummer's method. In this method, graphite undergoes oxidative treatment in the presence of strong acids and oxidizers.[55] Following this step, the mixture was initially neutralized by a strong base and then washed with ethanol in a centrifuge to remove excess acid. After washing with ethanol, three more washing cycles were done using DMF. In the washing procedure, the settled residual GO in the centrifugation tube was dispersed in fresh DMF. This mixture was run in a centrifuge for a set duration, typically around 20 mins. In the centrifugation process, the larger GO particles settled at the bottom of the tube, whereas small particles remained in the supernatant, producing a uniform suspension. The supernatant, which was a uniform PAN/GO suspension, was retrieved and added into additional DMF

and PAN, and stirred overnight, to produce a homogenous, well mixed PAN/GO/DMF solution. The particle size was not measured but was confirmed to be sufficiently small post-priori by the successful incorporation of the rGO into the fibers.

3.4. Material Fabrication

3.4.1. Electrospinning

Fibrous mats were fabricated using an in-house designed and built electrospinning setup shown in Figure 9.

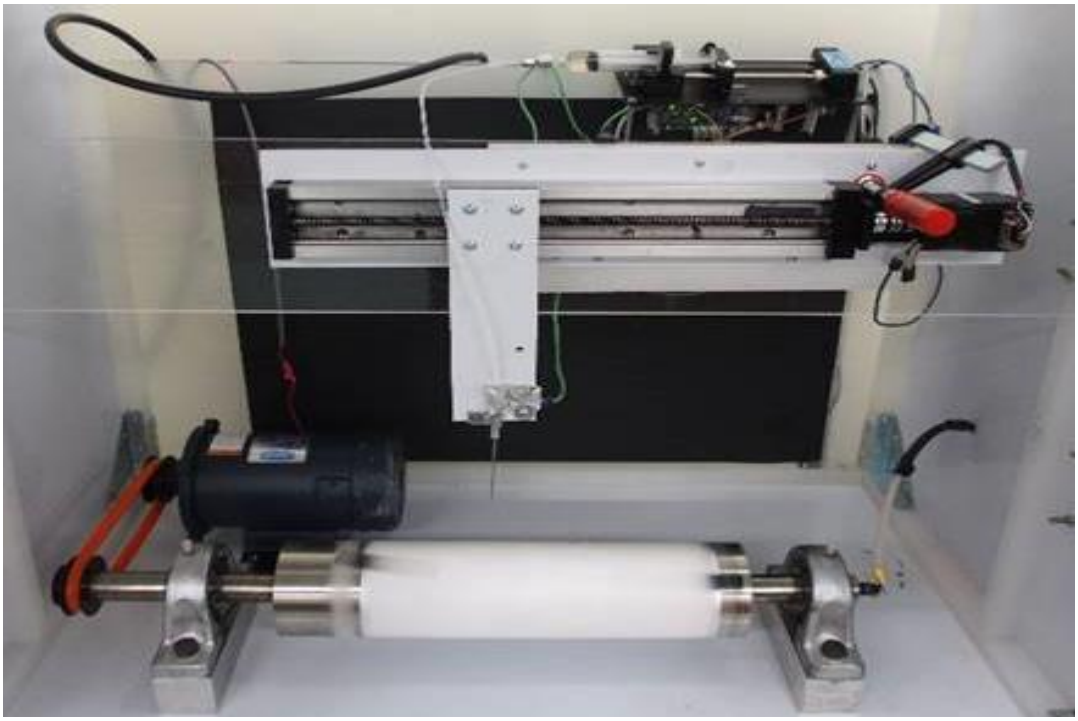

Figure 9: Electrospinning lab setup

The setup consisted of a syringe pump, which controlled the dispensing rate of the

polymer solution, a high voltage power supply and a rotating drum which also served as the collector. The needle was mounted on a linear motion platform to ensure a uniform sample could be obtained over the entire width of the collector drum. The high voltage power supply was connected to the needle and the collector was grounded during operation. During operation, the rotating drum was rotated at the lowest speed to ensure a random arrangement of fibers. Each electrospinning batch run produced a fibrous sheet with dimensions of 8.5" x 12", with thickness depending on the volume of the solution used for electrospinning. All solutions were electrospun using the conditions of the electrospinning apparatus, as summarized in Table 3. These electrospinning settings were taken from Liu, Kok, Kim, Barton, Brushett and Gostick (2017)[9] except for the flowrate.

Table 3: Electrospinning operational parameters

Parameter	Values
Voltage	15 kV
Voltage Polarity	Negative
Flowrate	0.3 – 0.5 mL/h
Needle Size	18 gauge (0.84 mm I.D.)
Needle – Collector Spacing	12.5 cm
Setup Atmosphere	Nitrogen
Temperature	Room Temperature ≈ 22 ℃

3.4.2. Carbonization

The electrospun mats were carbonized in a MTI GSL 1700X tube furnace (Figure 10). Electrospun mats, with size of 8.5" x 6", were folded twice and placed between two graphite plates. The graphite plates were crucial as they kept the electrodes flat and

compact, avoiding undesired shrinking and wrinkles on the surface.

Figure 10: MTI GSL-1700X tube furnace used for carbonization of PAN fibers

The heat profile selected for the carbonization was taken from Liu, Kok, Kim, Barton, Brushett and Gostick (2017)[9] (Figure 11). The heating rate in the carbonization process was maintained constant at 5 ℃/min. The electrospun mat was stabilized in air upto 250 ℃ and held isothermally at 250 ℃ for 2 hours, followed by introduction of nitrogen at flowrate of 150 sccm. The rest of the cycle was completed in a nitrogen atmosphere.

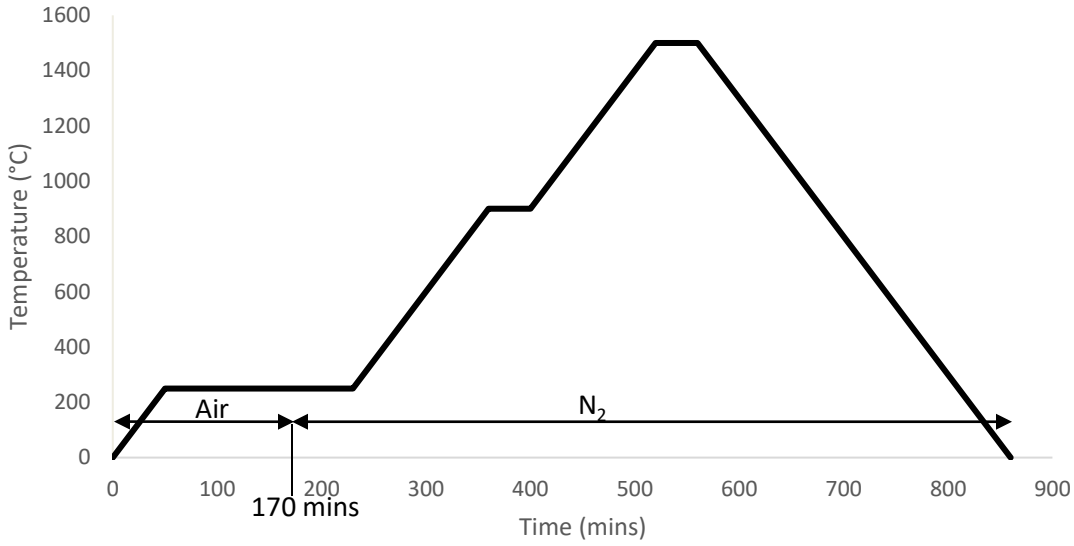

Figure 11: Heat profile for the carbonization process

3.5. Characterization

3.5.1. Scanning Electron Microscopy

The samples were characterized under a Quanta FEG250 scanning electron microscope to examine the fiber morphology and arrangement. The SEM images were taken from different locations and batches. Using SEM imaging software and produced images, the fiber diameter was measured five times at each location and then used to determine the average fiber diameter over entire mat.

3.5.2. In–Plane Electrical Conductivity

In–plane electrical conductivity was measured via the Van der Pauw method using an in-house built square probe arrangement electrical conductivity measuring device,

developed by Morris and Gostick (2012)[56] (Figure 12).

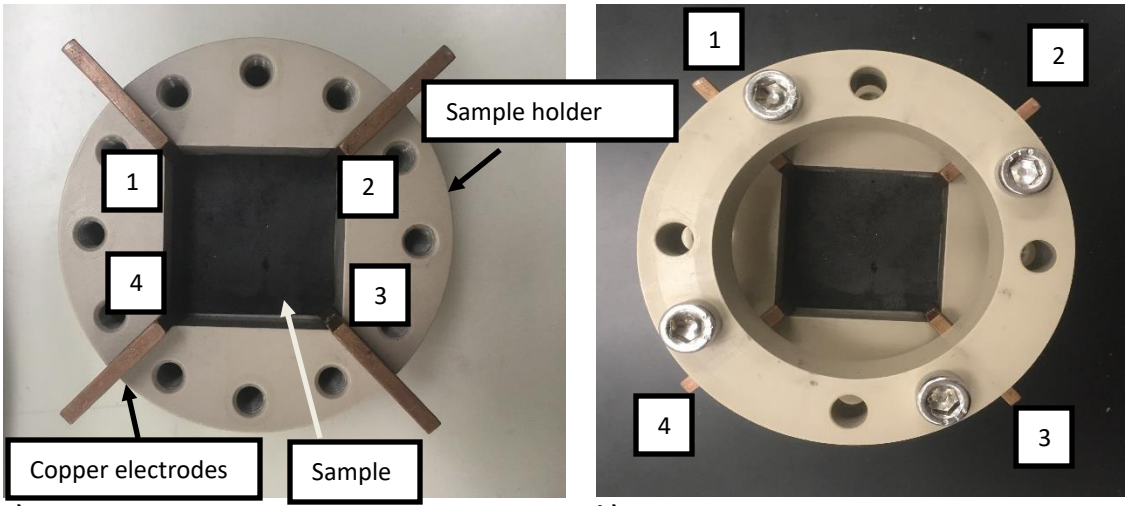

Figure 12: Electrical conductivity measuring device as described by Morris and Gostick (2012)[56] a) top view showing sample loading with four labelled copper electrodes placed at the corners b) assembled view

Samples were cut into 1" squares and placed in the holder. Four copper strips were placed on each corner of the square, acting as conductive contact points. A power supply was used to supply current on one edge of the square and a voltmeter was used to measure the voltage drop across the opposite edge. Voltage drop was measured across all edges of the sample. The experimental data was used to determine the resistance in the x and y direction using Eq. (3-1).

$$R_x = \frac{V_{34}}{I_{12}} \qquad R_y = \frac{V_{41}}{I_{23}} \tag{3-1}$$

where, R_x is the resistance in x direction, V_{34} is the voltage drop measured between point 3 and 4 and I_{12} is the current applied between points 1 and 2. Similarly, R_y is the resistance in the y-direction, V_{41} is the voltage drop measured between point 4 and 1 and I_{23} is the current applied at points 2 and 3. The sheet resistance, R_s, was calculated

by satisfying Van der Pauw equation (Eq. (3-2)): -

$$e^{-\left(\frac{\pi R_x}{R_s}\right)} + e^{-\left(\frac{\pi R_y}{R_s}\right)} = 1 \quad \textbf{(3-2)}$$

The bulk electrical conductivity, σ_{bulk}, was then calculated using Eq. (3-3): -

$$\sigma_{bulk} = \frac{1}{R_s t} \quad \textbf{(3-3)}$$

where t is the average thickness of the sample.

3.5.3. Porosity

Porosity was measured using the buoyancy technique as described by Rashapov, Unno and Gostick (2015)[37] (Figure 13). The buoyancy technique is an easy, quick and non-destructible technique, which measures the density of the solid phase in a porous medium.

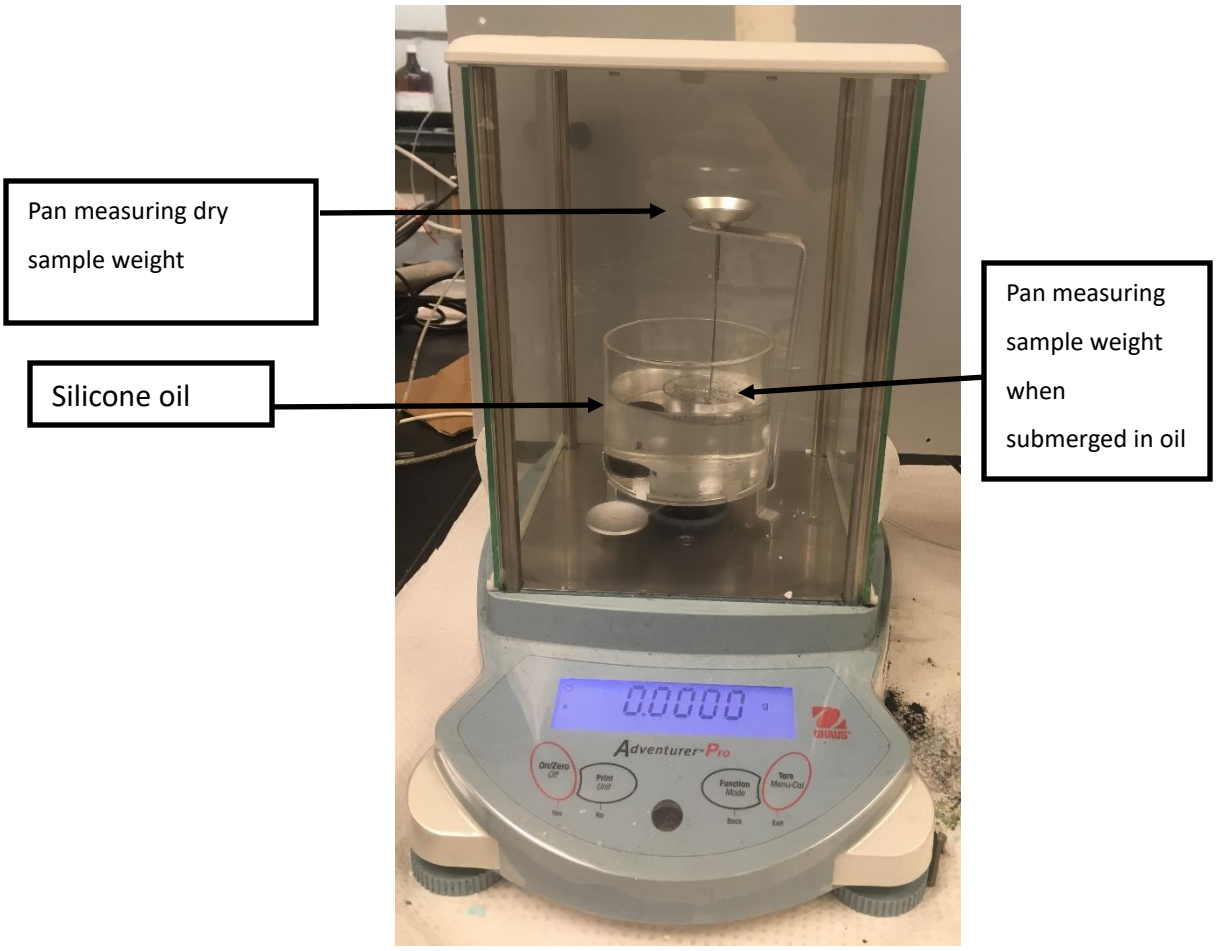

Figure 13: Porosity measurement device based on archimedes principle

A circular sample with $3/4$ " diameter is cut from the electrospun sheet. The thickness of the sample was measured using pressure sensitive screw gauge micrometer and dry weight of the sample are measured using high sensitive mass balance. The sample is then submerged in silicone oil due to its highly wetting nature, and the weight of the sample was measured, still submerged in the silicone oil tank. The solid phase density is determined using the Archimedes principle, shown in Eq (3-4): -

$$\rho_s = \rho_l \frac{m_{sa}}{m_l} = \rho_l \frac{m_{sa}}{m_{sa} - m_{sl}} \quad \textbf{(3-4)}$$

where, ρ_s is the solid phase density, ρ_l is the density of the liquid (silicone oil), m_l is the mass of liquid displaced, $m_{sa}\ and\ m_{sl}$ are the mass of the sample in air and submerged in liquid, respectively. The solid volume, V_s, and the porosity, ϵ, were determined using Eqs. (3-5)-(3-7).

$$V_s = \frac{m_{sa}}{\rho_s} \quad \textbf{(3-5)}$$

$$V_b = \pi r^2 t \quad \textbf{(3-6)}$$

$$\epsilon = 1 - \frac{V_s}{V_b} \quad \textbf{(3-7)}$$

where V_b is the bulk sample volume, r is the radius of the circular mat sample and t is the thickness of the sample.

3.5.4. In-plane permeability

In-plane permeability was measured using device developed by Gostick, Fowler, Pritzker, Ioannidis and Behra (2006)[57] (Figure 14).

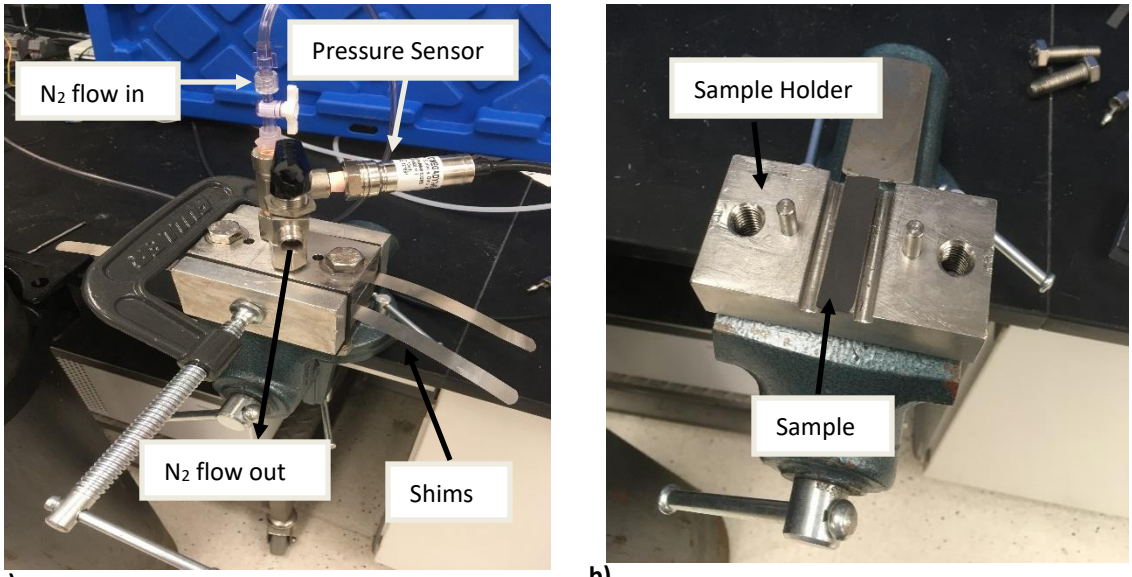

Figure 14: In-plane permeability device as described by Gostick, Fowler, Pritzker, Ioannidis and Behra (2006)[57] a) assembled view b) top view showing sample being loaded in the device

In-plane permeability was measured as function of compressed porosity, with permeability measurement fluid flowing through the thickness of the test sample. Each test sample, with dimensions 0.5" x 2", was placed between two plates. Feeler gauges of known thickness were placed between the two plates to control the compression of the test sample. Compressed nitrogen gas with flowrate controlled by MKS 1160B Series mass flow controller (range 0 – 200 sccm) was supplied at the inlet. The inlet pressure was measured using an Omega PX409-030A5V pressure sensor and the outlet was open to atmospheric pressure. Prior to every test, it was verified that no leaks and negligible pressure drop existed in absence of the sample in the test cell to ensure the observed pressure drop was associated with the test sample alone. Multiple runs were conducted for each sample with varying compression levels. Since the flowrate was restricted to

less than 200 sccm, no Forchheimer effect was observed. Given the use of a compressible fluid for these measurements (and no observable Forchheimer effect), the form of Darcy's Law used to determine the in-plane permeability is shown in Eq. (3-8): -

$$\frac{P_{in}^2 - P_{out}^2}{2LRT/MW_{N_2}} = \frac{\mu}{\kappa} m' \quad \textbf{(3-8)}$$

where $P_{in}\ and\ P_{out}$ are the inlet and outlet pressures, respectively, L is the length of the sample, R is the universal gas constant, T is the temperature, MW_{N_2} is the molecular weight of nitrogen, μ is the viscosity of nitrogen (taken as $1.73 \times 10^{-5}\ Pa.s$, and assumed to be independent of gas pressure), κ is the permeability coefficient and m' is the mass flux through the sample.

The Carmen – Kozeny (CK) is the most widely known permeability model which provides good predictions for all highly porous non-consolidated media.[57], [58] CK model which describes the dependence of permeability of a porous material on its porosity is shown in Eq. (3-9): -

$$K_{CK} = \frac{d_f^2 \varepsilon^3}{16 k_{CK} (1-\varepsilon)^2} \quad \textbf{(3-9)}$$

where K_{CK} is the permeability predicted by the CK model, d_f is the fiber diameter, ε is the porosity and $k_{CK}$is the CK constant. k_{CK} is used as a fitting parameter and depends on the type of media and alignment, arrangement and packing of fibers in a sample.

In order to compare the experimental data to CK permeability model, it is necessary to

convert the change in compressed thickness of the sample to change in porosity. Assuming that the compression of the sample only reduces the pore volume and that the sample only deforms in the direction of compression, the compressed porosity, ε_c, can be calculated using Eq. (3-10).

$$\varepsilon_c = 1 - \frac{1 - \varepsilon_0}{V_{bc}/V_{b0}} \quad \textbf{(3-10)}$$

where, ε_0 and V_{b0} is the bulk porosity and volume of the uncompressed sample and V_{bc} is the bulk volume of the compressed sample.

3.5.5. Through-plane permeability

The through-plane permeability was also measured using a device developed by Gostick Gostick, Fowler, Pritzker, Ioannidis and Behra (2006)[57] (Figure 15)

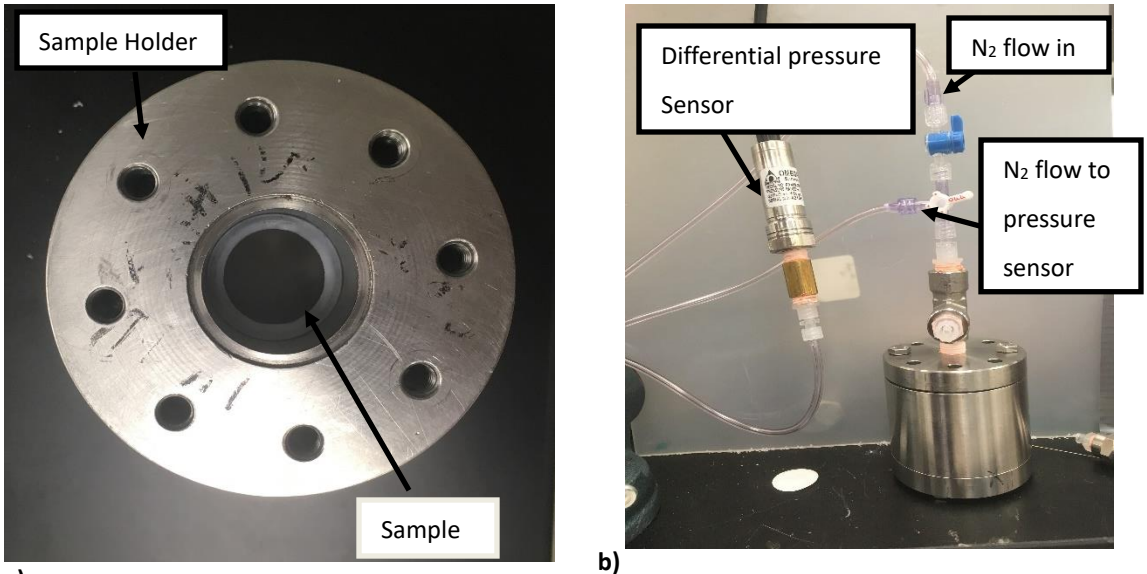

a) **b)**

Figure 15: Through-plane permeability measurement device as described by Gostick, Fowler, Pritzker, Ioannidis and Behra (2006)[57] a) top view showing sample loaded between two gaskets b) assembled view

A circular test sample, with 1” diameter, was placed in a holder between two gaskets. Gas is introduced on one side and made to flow through the surface of the sample at a fixed flow rate and the resultant pressure drop is measured. The test sample was secured, and a gas tight seal was achieved as low gas pressure (<15 Pa) was used during these experiments. The pressure drop was measured using an Omega PX653 differential pressure sensor and the flowrate was controlled using a MKS 1160B Series mass flow controller (range 0 – 200 sccm). The pressure drop was measured for varying flowrates. Eq. (3-8) was again used to determine the permeability coefficient from the measured pressure drop, but now L is defined as the thickness of the sample.

3.5.6. Specific Surface Area

The specific surface area of the samples was measured using vapor sorption analysis using DVS Resolution device acquired from Surface Measurement Systems (Figure 16).

Figure 16: Digital vapor sorption device used to measure specific surface area of fabricated samples

The samples were heat treated overnight, in an oven at 80 ℃ prior to testing to degas and remove any moisture adsorbed on the samples. Cyclohexane was used as the adsorbate and nitrogen was used as the carrier gas for cyclohexane vapors. Cyclohexane was chosen for its non-polar nature. Brunauer-Emmett-Teller (BET) theory was used to model the adsorption data and determine the specific surface area of the samples. BET

theory is represented using Eq. (3-11).

$$\frac{P/P_0}{n(1-P/P_0)} = \frac{C-1}{Cn_m}\left(\frac{P}{P_0}\right) + \frac{1}{Cn_m} \quad \textbf{(3-11)}$$

where n is the amount of cyclohexane adsorbed on the sample, n_m is the monolayer capacity of the adsorbed vapors, P is the pressure and P_0 is the saturation pressure of the adsorbate at the adsorption temperature and C is the BET constant.

A BET plot, which has $\frac{P/P_0}{n(1-P/P_0)}$ on the y axis and P/P_0 on the x axis, typically achieves a linear region between 5% - 30% partial pressure range, which is used to determine the specific surface area of the sample. However, linearity is not always restricted to this range. Hence, the BET results were validated using four thermodynamic criteria as described below[59]:

1. Monotonic increase of $n(1-P/P_0)$ as a function of P/P_0 in the selected pressure range.
2. Positive value for the BET parameter C resulting from linear regression.
3. The monolayer loading (n_m) should correspond to relative pressure within the selected pressure range.
4. Relative pressure corresponding to the calculated value for the monolayer formation $(1/\sqrt{C}+1)$ should be equal to the pressure determined from criterion 3.

3.5.7. 3-point bending test

3-point bend tests were conducted using a dynamic mechanical thermal analyzer from Rheometric Scientific (Figure 17).

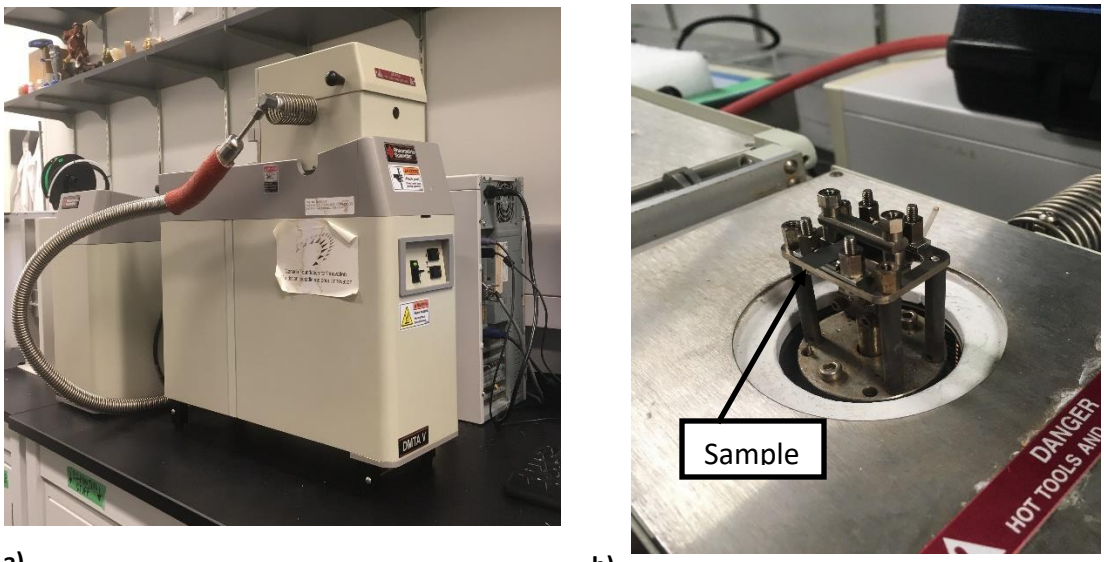

a) b)

Figure 17: Dynamic mechanical thermal analyzer used to conduct the 3-point bend test a) equipment b) smaple loaded in and ready for test

Samples were prepared with dimensions 3.5cm x 0.7cm were prepared and were tested at room temperature and a constant strain rate of $2 \times 10^{-5}\ s^{-1}$. Three sets of samples were tested for each material. Different materials were compared for their strain at break and flexural modulus (E_{flex}). Strain at break was determined from the stress strain curves, while, E_{flex}, was determined using the slope of the linear region in the stress strain curves.

4. Results & Analysis

4.1. Improving Transport Properties of Electrospun Electrode

This part of the thesis will discuss work done to increase the power density and efficiency of a flow battery by improving the electrical conductivity of material to match that of commercially available electrodes. The results will be compared to that of Liu, Kok, Kim, Barton, Brushett and Gostick (2017)[9] and commercially manufactured electrodes. The electrospun mats fabricated were formed from 10 wt% PAN/DMF solutions. The PAN/DMF composition was selected as it produces a consistent fiber diameter of ~500 nm, without the formation of beads in the fibers.

4.1.1. SEM Imaging and Fiber diameter

This section will present SEM images and determine the average fiber diameter for materials fabricated using different approaches to improve electrical conductivity of the electrospun mats. The first approach used to improve the electrical conductivity was to increase the carbonization temperature and stabilization time in the carbonization cycle. The carbonization temperature was increased from 1100 ℃ to 1500 ℃ and the stabilization time was increased from 1 hour to 2 hours. Figure 18 shows SEM images of electrospun mats prior to and after carbonization at 1100 ℃ and 1500 ℃. The stabilization time used for both the temperatures was 2 hours

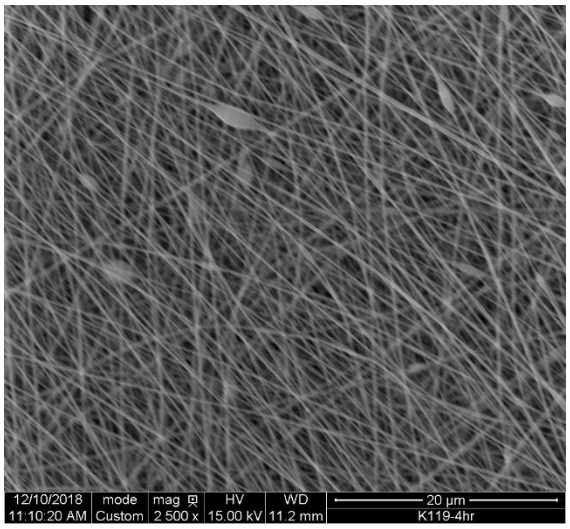

a)

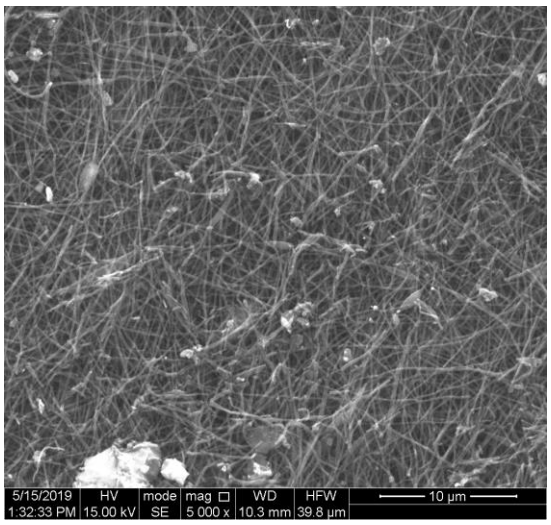

b)

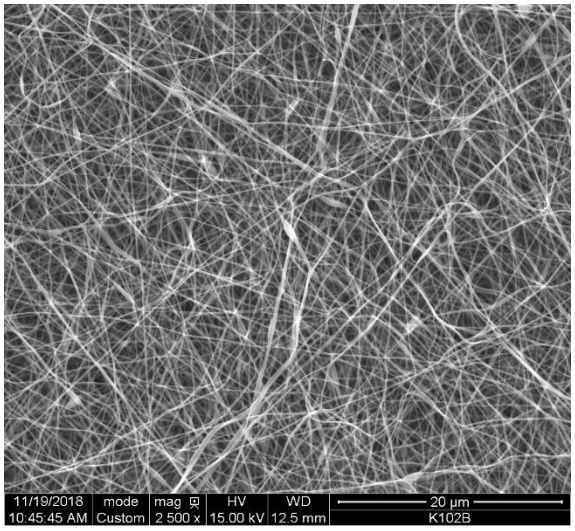

c)

Figure 18: SEM images for a) Electrospun PAN fibers b) carbonized at 1100 °C c) carbonized at 1500 °C showing no fiber morphological changes by using a higher carbonization temperature except for fiber diameter.

The SEM images show that the carbonization process significantly decreases the fiber diameter. Liu, Kok, Kim, Barton, Brushett and Gostick (2017)[9] reported a 28% decrease in fiber diameter after carbonization. Increasing the carbonization temperature and the stabilization time also reduced the fiber diameter by ~30%. An increase in the

carbonization temperature has no other effect on the fiber morphology. This approach will be used cumulatively with the other two approaches to study their impact on electrical conductivity.

The second approach was to introduce the additive graphene into the fibers. A PAN/DMF solution containing 3 wt% GO was prepared and electrospun. The 3 wt% GO loading was selected as suggested by Tsai, Yang, Ma, Xie (2011)[60] Using this approach some graphene particles were not integrated into the fiber matrix due to size mismatch. At this weight percent, the graphene particles agglomerated into blobs in the fiber matrix during the carbonization process, as shown in Figure 19b.

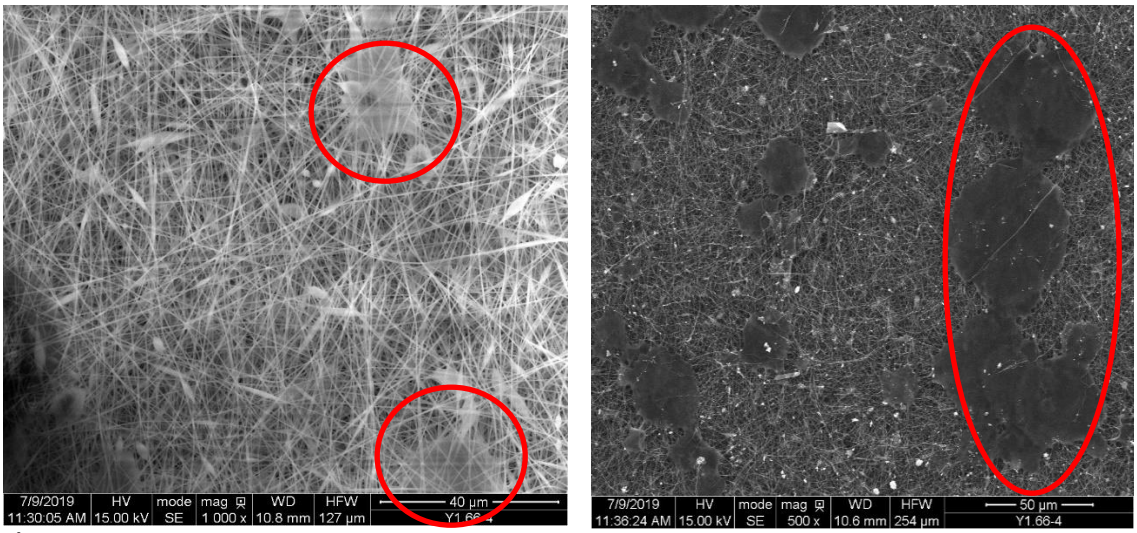

a) b)

Figure 19: SEM images for PAN with 3wt% GO loading a) before carbonization showing agglomeration of GO particles and not integrated into the fibers b) carbonized PAN/GO fibers emphasizing the problem due to agglomerated particles between fibers

As 3wt% proved to be the threshold loading of GO in the electrospinning solution, a

solution with 0.5wt% lower GO loading was chosen to be prepared for electrospinning using a design of experiment approach. Figure 20 shows SEM images of PAN fibers formed with 2.6wt% GO loading prior to and after carbonization. Using solution with low GO loading, the fibers were successfully electrospun with no blob formation between the fibers. PAN/Graphene fibers prepared using 2.6 wt% GO loading in the polymer solution was further characterized. The average diameter of PAN/GO fibers was approximately 275 nm, 1.5 times that of PAN fibers. The increase in fiber diameter is mainly due to the introduction of GO particles in the solution. The fiber diameter was halved in the carbonization process and was slightly higher compared to carbonized PAN fibers.

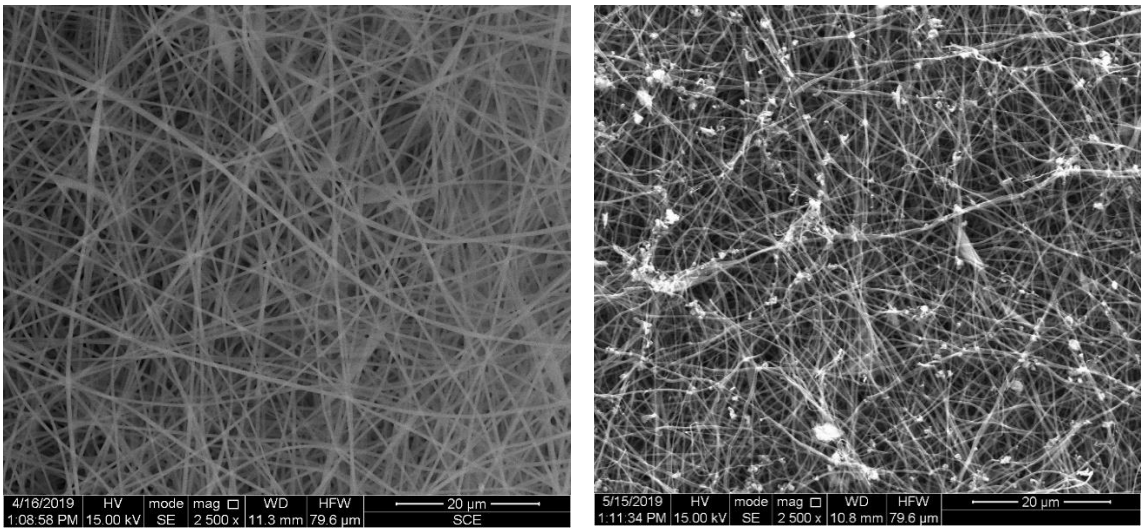

a) **b)**

Figure 20: SEM images for PAN fibers with 2.6 wt% GO loading a) uncarbonized with GO particles well integrated into the fibers as GO particles were not agglomerated between fibers b) carbonized at 1500 °C

The third approach in this study was to expose PAN fibers to DMF vapor. As PAN fibers

are soluble in DMF, the vapors will soften the fibers and allow them to initiate new inter-fiber contacts and increase the contact area between pre-existing contacts. The SEM images produced via this approach, prior to and after carbonization, are shown in Figure 21. Figure 21a show that the DMF treatment has made fibers compact, caused some fibers to merge, increasing contact area between them, and new contacts have initiated between some fibers. After carbonization, the PAN fibers treated with DMF vapor experienced similar decrease in fiber diameter as compared to untreated PAN fibers as the chemical nature of the fibers are unchanged and no additions have been made to the fiber matrix.

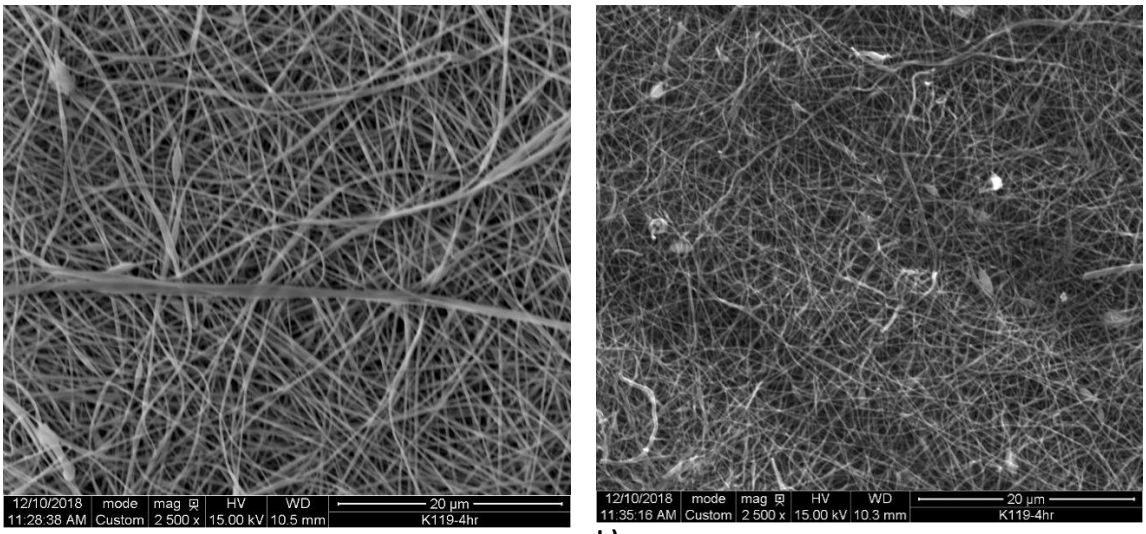

a) **b)**

Figure 21: SEM images of PAN fibers exposed to DMF vapor a) before carbonization showing compactness and merging of fibers b) carbonized at 1500 °C

The average fiber diameters using different approaches are summarized in Table 4. Note that the electrospinning process can produce different results with subtle changes in

conditions. For instance, the solution used for electrospinning in this study contained the same weight percent of polymer as that of Liu, Kok, Kim, Barton, Brushett and Gostick (2017)[9], who produced electrospun mat with fibers having twice the diameter. The main reason for this is the use of a different size needle to fabricate fibers and different flowrates used during electrospinning.

By comparison, the SGL25AA and Toray 90 commercial electrodes have average fiber diameter of 7 – 8 μm[9], which is 35 times larger than that of untreated and carbonized PAN fibers fabricated in this study.

Table 4: Summary of average fiber diameter of commercial and developed electrodes

Fiber	Electrospun d_f (nm)	d_f after carbonization (nm)
SGL25AA	-	7330
Toray 90	-	7720
Liu et al.[9]	700 ± 300	500 ± 170
High Carbonization Temp.	300 ± 50	213 ± 60
PAN/Graphene	560 ± 75	275 ± 35
PAN exposed to DMF	250 ± 45	175 ± 40

4.1.2. Porosity

The porosities of the materials fabricated in this study and commercially fabricated electrodes were measured and compared. Each of the approaches described above had little to no effect on the porosity of the carbonized electrode. The commercial electrode, SGL25AA electrode has a similar porosity as compared to electrospun PAN fibers, while Toray 90 is 14% less porous, indicating presence of more solid mass and lesser pore volume. Figure 22 shows a summary of the porosities of the different materials in this

study. Note that the high porosity of the SGL25AA material is due to a porous carbonized binder added to the matrix, which is not necessarily useful for flow cells since these pores are very small and do not enhance fluid flow. The high porosity values obtained in the present samples represent truly useful porosity comprised of large pores.

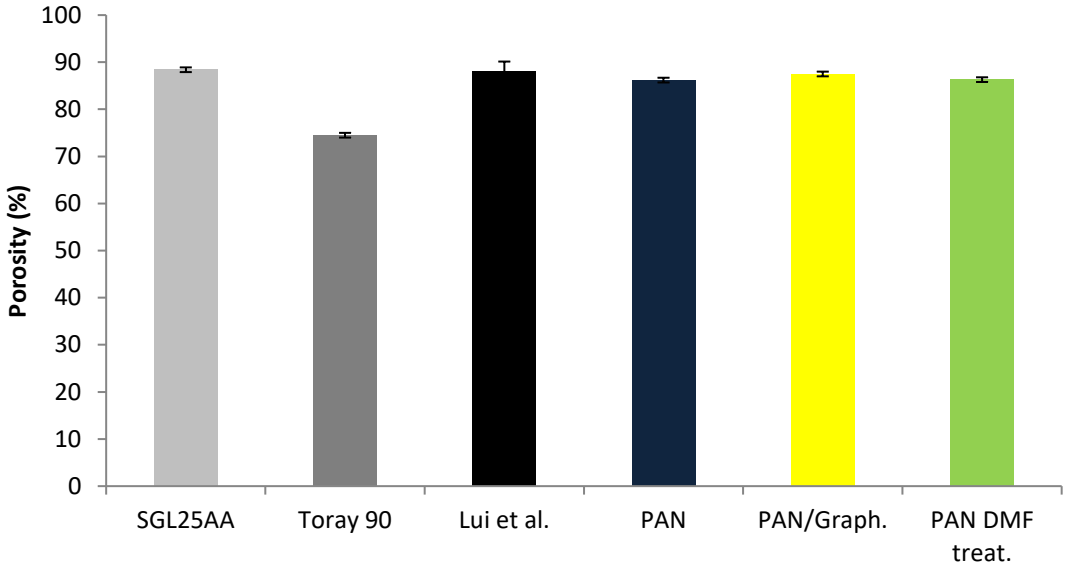

Figure 22: Comparison of porosities of developed and commercial electrodes

4.1.3. Electrical Conductivity

The electrical conductivity was measured in the in-plane direction for fabricated materials and compared with that of commercial electrodes. The electrical conductivity of electrospun PAN electrodes fabricated by Liu, Kok, Kim, Barton, Brushett and Gostick (2017)[9] was found to be 1519 S/m. Increasing the carbonization temperature from 1100 °C to 1500 °C for our samples increased the electrical conductivity to a value of 3430 S/m, which represents an increase of 125% compared to electrodes fabricated by

Liu, Kok, Kim, Barton, Brushett and Gostick (2017)[9] Higher carbonization temperature increases the graphitic nature of the fibers, making them more electrically conductive. The higher carbonization temperature was also used with other two approaches used to increase electrical conductivity.

Graphene oxide (GO) was used as an additive in the fiber matrix to increase the electrical conductivity. GO is partially to reduced GO (rGO) during the carbonization process. The addition of graphene, a material known for its exceptional electrical conductivity, further increased the graphitic content of the fiber matrix, resulting in an increase of the electrical conductivity to 3910 S/m, which represents a 157% increase compared to that of Liu, Kok, Kim, Barton, Brushett and Gostick (2017)[9] and a 14% increase compared to the untreated PAN fibers fabricated in this study.

PAN fibers exposed to DMF vapor created new contacts between fibers and increased contact surface area between existing contacts. This technique resulted in the highest increase in electrical conductivity, corresponding to an 180% increase in electrical conductivity compared to that of Liu, Kok, Kim, Barton, Brushett and Gostick (2017)[9] and 44% increase compared to untreated PAN electrodes fabricated in this study.

The results obtained in this section were further compared to the electrical conductivities of commercial electrodes, SGL25AA and Toray 90. All the electrodes

fabricated in this study surpassed the electrical conductivity of the widely used SGL25AA electrode. Toray 90 has an electrical conductivity that is approximately 5 times larger than that of various PAN fibers fabricated in this study. However, a comparison between Toray 90 and all other developed and commercial electrodes mentioned is unbalanced. Toray 90 has roughly 15% less porosity compared to all other developed and commercial electrodes in this study, which shows presence of more solid mass. The presence of solid mass is mainly associated to binders present between fibers as shown in Figure 23. The binders increase the electron flowing paths, increasing the overall conductivity of the fibers.

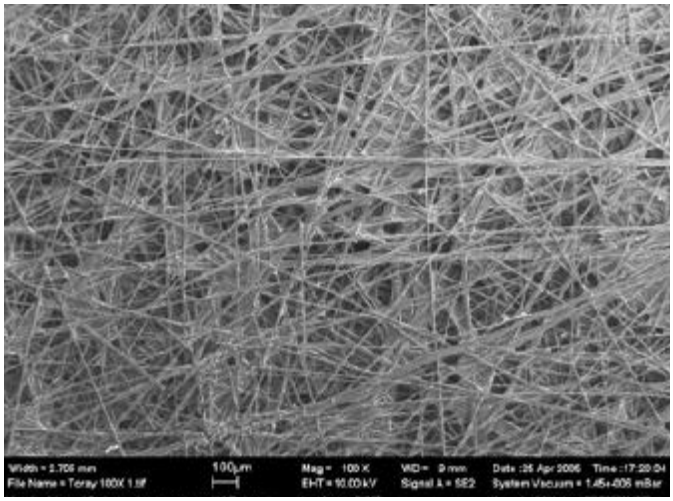

Figure 23: SEM image for Toray 90 showing the presence of binders in the fiber matrix which promotes efficient electron flow

The electrical conductivities obtained in this study are summarized Figure 24.

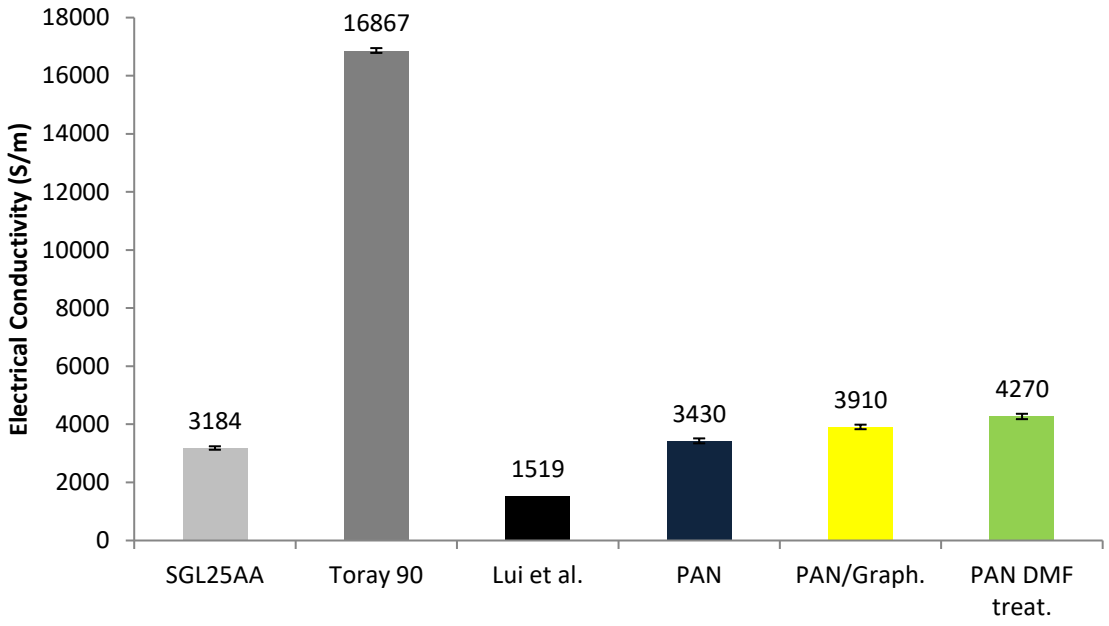

Figure 24: Comparison of electrical conductivities of commercial and developed PAN fibers using different approaches

4.1.4. Specific Surface Area

The specific surface area was measured using a digital vapor sorption (DVS) system for this study with cyclohexane used as adsorbate. The data available for Liu, Kok, Kim, Barton, Brushett and Gostick (2017)[9] were measured using gas sorption analysis with nitrogen gas at 77 °K. Lack of availability of samples fabricated by Liu, Kok, Kim, Barton, Brushett and Gostick (2017)[9] and commercial electrodes, this section will only report specific surface area data for PAN fibers fabricated using different approaches in this study. Figure 25 summarizes the results obtained for this section. The approach in which PAN fibers are exposed to DMF vapor in order to improve electrical conductivity, slightly decreased the specific surface area of the electrode as compared to that of untreated

PAN. Exposure to DMF vapors caused some fibers to merge, decreasing the number of active sites as a result.

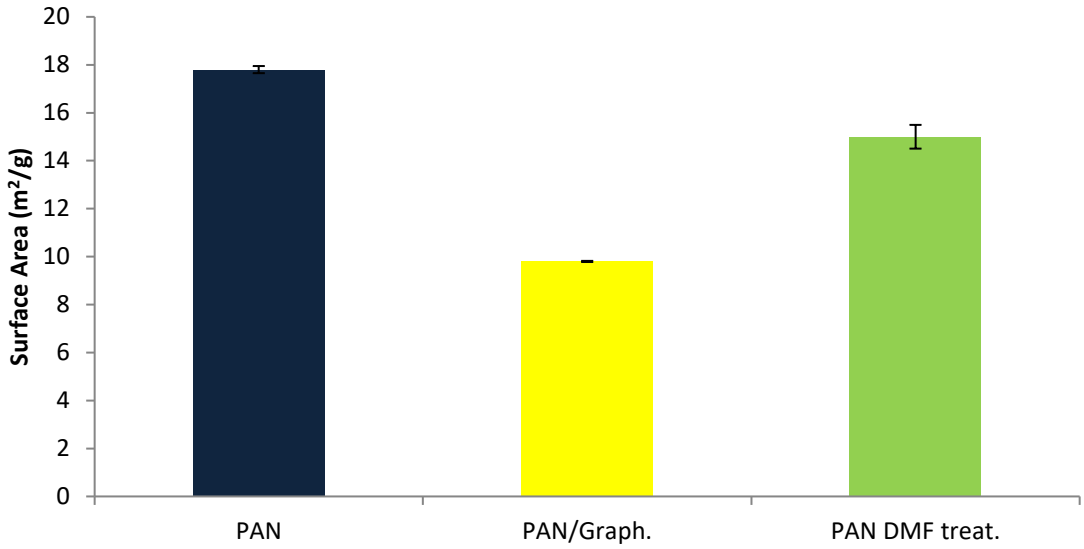

Figure 25: Comparison of specific Surface Area of electrodes fabricated using different approaches

A decrease was also observed in the specific surface area of PAN fibers with graphene integrated into the fibers as compared to untreated PAN fibers. This is mainly associated with the larger fiber diameter in the PAN/graphene electrodes. As fiber diameter increases, the number of adsorption sites per unit volume decreases, resulting in lower specific surface area.

4.1.5. In-plane Permeability

The in-plane permeability coefficient K_{IP} was measured as a function of compressed porosity for the PAN fibers fabricated in this study. Lack of availability of samples fabricated by Liu, Kok, Kim, Barton, Brushett and Gostick (2017)[9] and commercial

electrodes, this section will only report in-plane permeability data for PAN fibers fabricated using different approaches in this study. As the material is compressed, the pore spaces reduce and flow in the plane direction is restricted and reduced, causing the permeability to decrease. This behavior was observed for all the materials tested in this section. Figure 26 summarizes these results. The in-plane permeability coefficients of untreated PAN and PAN/graphene fibers reduce to a similar value of $\sim 4.4 \times 10^{-13} m^2$ at 78% compressed porosity. However, PAN fibers exposed to DMF vapors experienced a larger reduction of the in-plane permeability coefficient. Untreated PAN and PAN/graphene fibers are fluffier in nature and the fibers are less compact. When exposed to DMF vapor, the uncarbonized PAN fibers were sandwiched between porous plates and exposed to DMF atmosphere. Due to this compression and the softening effect from the DMF vapors, the fibers come together and become compact. Upon compression during the in-plane permeability test, the in-plane permeability coefficient is reduced significantly.

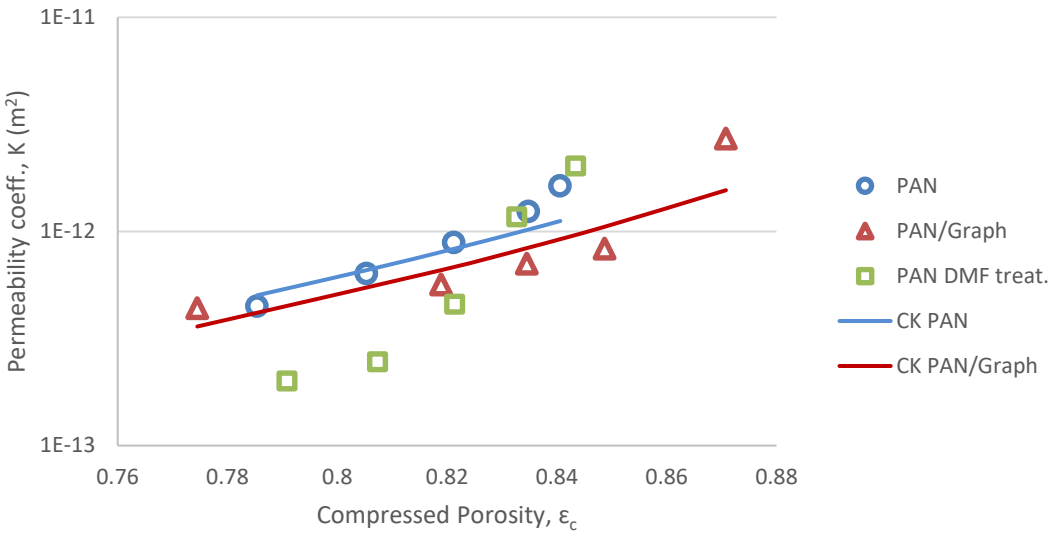

Figure 26: Comparison of in-plane Permeability of PAN fibers fabricated in this study using different approaches with compressed porosity on the x-axis and in-plane permeability coefficient on the y-axis.

Carmen-Kozeny relationship (Eq. (3-9)), was used to fit the data and to determine the Carmen-Kozeny constant, k_{ck}. k_{ck} is a fitting parameter and depends on the type of media and is independent of porosity and fiber size, so provides a means of comparing materials that may be similar in structure but have slightly different overall properties.[57] k_{ck} value was determined to be 0.04 for untreated PAN fibers and 0.12 for PAN/graphene fibers. Using the Carmen-Kozeny model and determined k_{ck} value, the permeabilities of the uncompressed and untreated PAN fibers and PAN/graphene fibers are predicted to be $1.6 \times 10^{-12}\ m^2$ and $1.7 \times 10^{-12}\ m^2$, respectively. The k_{ck} value for PAN fibers exposed to DMF vapor changed with increasing compression, but levelled off after 81% compressed porosity, as shown in Figure 27. This is unusual but may be due to fiber breakage during compression which effectively changes the

morphology of the medium.

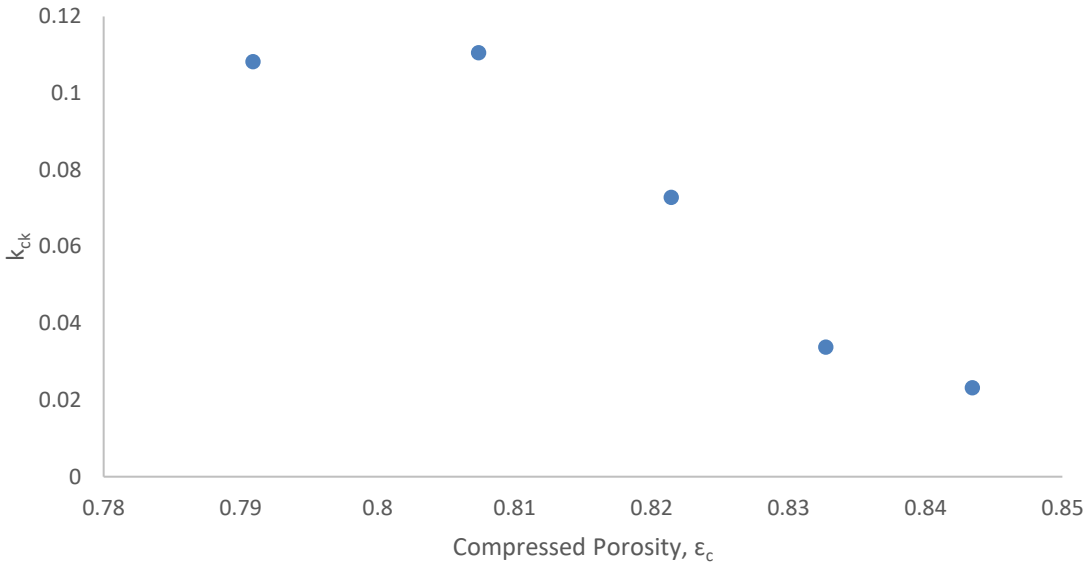

Figure 27: Effect of compression on k_{ck} for PAN fibers exposed to DMF vapor

4.1.6. Through plane permeability

The through plane permeability coefficient K_{TP} was measured for PAN fibers fabricated in this study. Lack of availability of samples fabricated by Liu, Kok, Kim, Barton, Brushett and Gostick (2017)[9] and commercial electrodes, this section will only report through-plane data for PAN fibers fabricated using different approaches in this study. Figure 28 summarizes the data obtained for the different materials. The through-plane permeability of untreated PAN fibers and PAN fibers exposed to DMF are similar, with PAN fibers exposed to DMF slightly higher. The slightly higher value is due to the compactness of the fibers. Exposure to DMF brings the PAN fibers closer to each other making the path of fluid flow less tortuous.

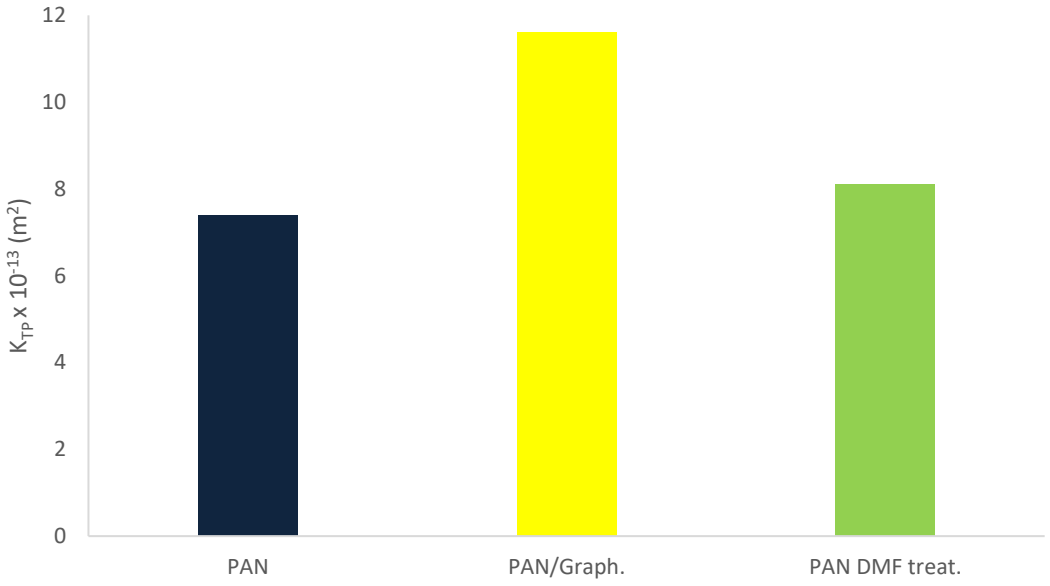

Figure 28: Comparison of through plane permeability for electrodes fabricated in this study

PAN/graphene fibers have higher K_{TP} as compared to that of the other two materials. PAN/graphene have a higher fiber diameter, which corresponds to fewer fibers in specific volume than that of electrodes with thinner fibers. Thus, thee fluid flowing through the fibers experience less resistance, i.e. lower tortuosity, and higher K_{TP} value.

4.2. Improving Mechanical Integrity of Electrospun Electrodes

Carbon fibers have been widely used commercially for applications requiring high strength materials. Use of carbon fibers has been widely integrated in the aerospace, military, automobile and sports industries. High strength carbons are usually produced by passing a single strand of PAN through a furnace so that it is carbonized under tension. Carbonizing each fiber strand under tension is not possible with electrospun mats, which makes their general nature brittle. The brittle nature of electrodes is undesirable for flow battery applications. Thus, improvement of the mechanical property of the PEL is key for the development and long term operation of flow batteries.[61]–[63]

This part of the thesis compares the mechanical integrity of two commercial electrodes with that of the in-house fabricated electrodes. The in-house developed electrodes include those fabricated using the different methods to achieve the first objective and the commercial electrodes include Toray 120 and Freudenberg with 0% PTFE loading. The 3-point bending, or flexural test was used to study the mechanical integrity of the electrodes, using flexural modulus and strain at break as points of comparison.

4.2.1. Flexural Modulus

Flexural modulus was derived from the slope of the linear region in the stress strain curves obtained from the 3-point bending test. Some sample data for such test are shown in Figure 29.

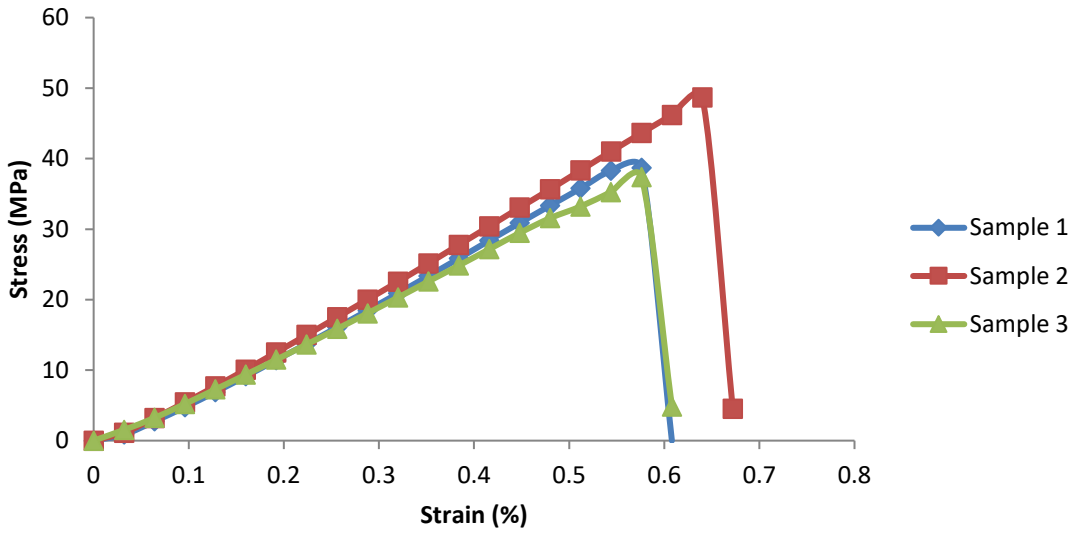

Figure 29: Raw data of stress-strain curves for untreated PAN electrode

Figure 30 summarizes the results obtained for this section. The Freudenberg sample has the lowest flexural modulus, while untreated PAN exhibits the highest flexural modulus. The two approaches used to improve the electrical conductivity reduced the flexural modulus by $\sim 60\%$. However, having a low flexural modulus is not a definitive disadvantage. Materials with low flexural modulus and high strain can be manufactured in spools rather than in sheets. A more critical feature is the ability of the materials to experience strain without breaking, as discussed in the next section.

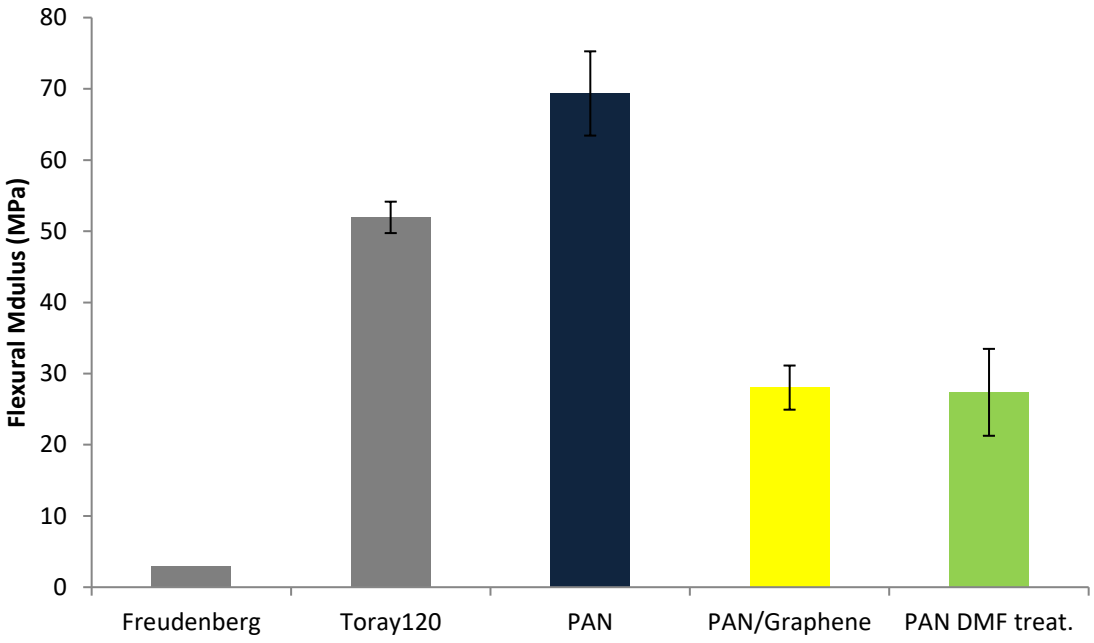

Figure 30: Comparison of flexural modulus for electrodes fabricated in this study and commercial electrodes

4.2.2. Strain at break

The data for strain at break or failure is shown in Figure 31. The Freudenberg samples, which are hydroentangled and flexible (to the point of being barely self-supporting) did not fail, consequently, the test was stopped as it reached the maximum stage time, and so the Freudenberg sample is not included in Figure 31. PAN fibers exposed to DMF vapor exhibits the lowest strain at break, while Toray 120, untreated PAN and PAN/Graphene fibers show similar strain at break. All electrodes tested in this section except Freudenberg are brittle in nature.

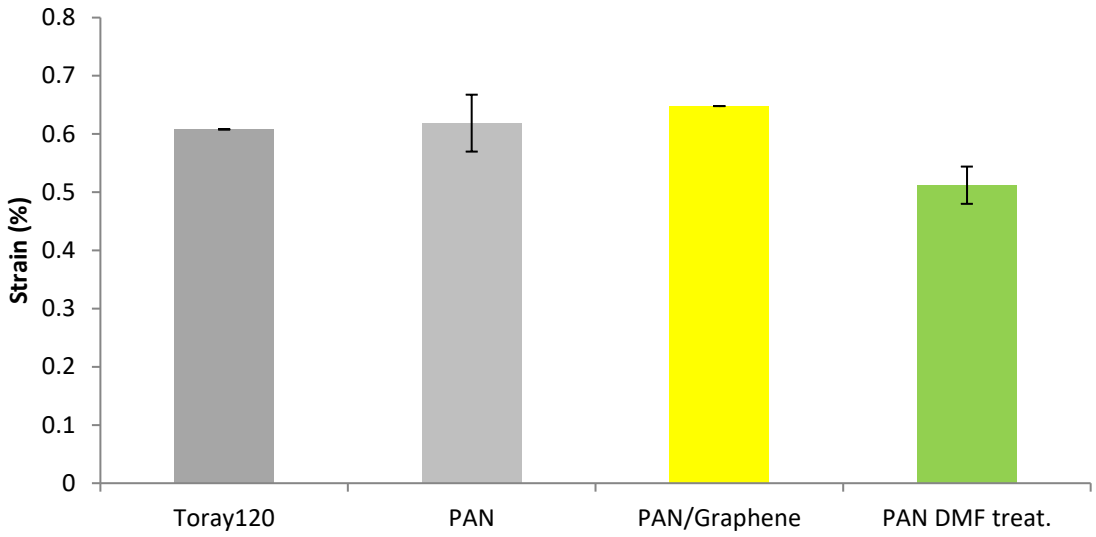

Figure 31: Comparison of strain at break of electrodes developed in this study and commercial electrodes.

Having a similar breaking point as Toray is highly encouraging as the material is regularly used in fuel cells which are also compressed. This indicates that the present materials may be sufficiently tough for use in flow cells, although the fact that ordinary PAN has the same strength as Toray is unexpected since the in-house materials seem qualitatively more fragile. This contradiction suggests that a different mechanical test may be more suitable for assessing this mechanical property.

4.3. Summary of Results

Table 5: Summary of Results for Part 1

Material / Characterization	SGL25AA	Toray90	Lui et al. [9]	PAN	PAN/Grap	PAN DMF treat.
d_f (nm), carbonized	7330	7720	500	213	275	175
Porosity (%)	88.4	74.5	88.65	86.2	87.5	86.3
Electrical Conductivity (S/m)	3184	16867	1519	3430	3910	4270
In plane Permeability x10^{-12} (m^2)	_	_	_	1.6	1.7	_
Through plane Permeability x10^{-13} (m^2)	_	_	_	7.4	11.6	8.1
Sp. Surface Area (m^2/g)	_	_	_	17.8	9.8	15

Table 6: Summary of results for Part 2

Material / Characterization	Freudenberg	Toray120	PAN	PAN/Grap	PAN DMF treat.
Flexural Modulus (MPa)	3	52	69	28	27
Strain at break (%)	No break	0.61	0.62	0.65	0.51

5. Conclusions

The thesis focused on achieving two objectives. The first objective was to improve the electrical conductivity of the PEL with the ultimate intention of increasing the power density and the efficiency of the flow battery system. Three routes were undertaken to achieve this objective. The first route was to increase the carbonization temperature. Increasing the carbonization temperature, raised the electrical conductivity by 125% compared to that reported by Liu, Kok, Kim, Barton, Brushett and Gostick's[9]. Other key properties such as porosity, permeability and surface area were not affected by the change in carbonization temperature. Higher carbonization temperature was used with the other two approaches.

The second approach used to improve electrical conductivity of the GDL was to incorporate an additive, graphene, in the fibers. Graphene was successfully incorporated within the fibers without any blob formation. The fiber diameter of PAN/GO fibers was almost 2 times the fiber diameter of PAN fibers. During carbonization, the fiber diameter was reduced by 50%, which is more than that experienced by untreated PAN. The electrical conductivity for PAN/graphene fibers increased by 157% compared to that of Liu, Kok, Kim, Barton, Brushett and Gostick[9]. As the fiber diameter increased, the permeability of the fibers increased, and the specific surface area decreased. The porosity was unaffected by the addition of graphene to the fiber matrix.

The third route undertaken to improve the electrical conductivity was to sinter PAN fibers by exposing them to DMF vapor. As PAN is soluble in DMF, DMF vapor soften the fibers and bring them closer, initiating new inter-fiber contacts and increasing the contact area between pre-existing contacts. This route yielded the highest electrical conductivity, ~180% more than that of Liu, Kok, Kim, Barton, Brushett and Gostick (2017) [9]. The high electrical conductivity using this approach came at the cost of the in-permeability of the material. The in-plane permeability drastically dropped with slight compression, which suggests PAN/graphene may be a better overall approach and yield better flow cell performance.

The second objective of the thesis was to study the mechanical integrity of the developed material. To study the mechanical integrity, the developed materials were compared for flexural modulus and strain at break. The flexural modulus data showed that untreated PAN fibers had the highest modulus and the other two approaches reduced the flexural modulus by 60%, showing the electrodes are easier to bend or deflect. As for strain at break, all the materials exhibited similar strain at break.

6. Future Works

In order to validate the developments made in this study, the fabricated materials must be tested in a redox flow cell lab scale setup. The results from the flow cell test will give a sense of the extent of improvement achieved by this study.

Although the electrical conductivity of the PEL was successfully improved, more paths to further enhance the electrical conductivity of the PEL can be explored. A very high carbonization temperature (>2000 °C) will increase the degree of graphitization of carbonized PAN fibers. Higher degree of graphitization will improve the quality of the fibers, increase electrical conductivity and make the fibers more rigid and tough.[64]

Toray 90 exhibited the highest electrical conductivity measurement among all the electrodes tested. One reason for the high electrical conductivity is the presence of a binder between the fibers (SEM image shown in Figure 23). The binders make the electron transfer more efficient resulting in 4 times the electrical conductivity as compared to best performing electrode developed in this study. The recommendation would be to explore methods to incorporate the binder with the fibers. One method of achieving that would be to treat carbonized PAN fibers by dipping them in a PAN/DMF solution and slowly evaporating the solution from the fibers in a controlled environment. As DMF slowly evaporates from the fibers, it leaves behind PAN that will act as a binder between fibers. A thorough optimization is required as to how much pore space needs

to be filled with PAN so that other key properties and overall performance of the flow cell is not negatively affected.

A further thorough study needs to be done on improving the mechanical integrity of the electrodes. Although an increase in the carbonization temperature is one way to make the fibers more rigid and tough, however, methods to make the electrode flexible should also be explored.

7. References

[1] Enerdata, “World Energy Consumption Statistics 2019,” *Global Energy Statistical Yearbook 2019*, 2019. [Online]. Available: https://yearbook.enerdata.net/total-energy/world-consumption-statistics.html. [Accessed: 15-Jul-2019].

[2] International Energy Agency, “GECO 2019,” *Global Energy & CO2 Status Report*, 2019. [Online]. Available: https://www.iea.org/geco/. [Accessed: 15-Jul-2019].

[3] International Energy Agency, “Energy Access Database,” 2016. [Online]. Available: https://www.iea.org/energyaccess/database/. [Accessed: 15-Jul-2019].

[4] International Energy Agency, “Statistics,” 2019. [Online]. Available: https://www.iea.org/statistics/?country=WORLD&year=2016&category=Electricity&indicator=undefined&mode=chart&dataTable=INDICATORS. [Accessed: 15-Jul-2019].

[5] N. Oreskes, “Beyond the Ivory Tower: The scientific consensus on climatic change,” *Science*. 2004.

[6] H. Ibrahim, A. Ilinca, and J. Perron, “Energy storage systems-Characteristics and comparisons,” *Renew. Sustain. Energy Rev.*, vol. 12, no. 5, pp. 1221–1250, 2008.

[7] W. Wang, Q. Luo, B. Li, X. Wei, L. Li, and Z. Yang, “Recent Progress in Redox Flow Battery Research and Development,” pp. 970–986, 2013.

[8] B. Dunn, H. Kamath, and J. M. Tarascon, “Electrical energy storage for the grid: A battery of choices,” *Science (80-.).*, vol. 334, no. 6058, pp. 928–935, 2011.

[9] S. Liu, M. Kok, Y. Kim, J. L. Barton, F. R. Brushett, and J. Gostick, “Evaluation of

Electrospun Fibrous Mats Targeted for Use as Flow Battery Electrodes," *J. Electrochem. Soc.*, vol. 164, no. 9, pp. A2038–A2048, 2017.

[10] S. Yadav, "Fabrication and Characterization of Novel Flow Battery Electrodes using Electrospinning," 2018.

[11] Z. Zhou *et al.*, "Development of carbon nanofibers from aligned electrospun polyacrylonitrile nanofiber bundles and characterization of their microstructural, electrical, and mechanical properties," *Polymer (Guildf).*, vol. 50, no. 13, pp. 2999–3006, 2009.

[12] S. Y. Gu, J. Ren, and G. J. Vancso, "Process optimization and empirical modeling for electrospun polyacrylonitrile (PAN) nanofiber precursor of carbon nanofibers," *Eur. Polym. J.*, vol. 41, no. 11, pp. 2559–2568, 2005.

[13] L. Zhang, A. Aboagye, A. Kelkar, C. Lai, and H. Fong, "A review: Carbon nanofibers from electrospun polyacrylonitrile and their applications," *J. Mater. Sci.*, vol. 49, no. 2, pp. 463–480, 2014.

[14] K. Tse-Hao, Y. Ching-Chyuan, and C. Wen-Tong, "The effect of stabilization on the properties of PAN-based carbon films," *Carbon N. Y.*, vol. 31, no. 4, pp. 583–590, 1993.

[15] P. F. Ribeiro, B. K. Johnson, M. L. Crow, A. Arsoy, and Y. Liu, "Energy Storage systems for Advances Power Applications," *Proc. IEEE*, vol. 89, no. 12, pp. 1744–1756, 2001.

[16] K. V Vidyanandan, "K. V. Vidyanandan, 'Role of Energy Storage in the Grid

Integration of Wind and Solar PV Energy Systems', Global Energy Technology Summit (GETS)-2014, pp. 1-13, New Delhi, India, 7-...," no. March, pp. 1–13, 2016.

[17] H. Chen, T. N. Cong, W. Yang, C. Tan, Y. Li, and Y. Ding, "Progress in electrical energy storage system: A critical review," *Prog. Nat. Sci.*, vol. 19, no. 3, pp. 291–312, 2009.

[18] M. Aneke and M. Wang, "Energy storage technologies and real life applications – A state of the art review," *Appl. Energy*, vol. 179, pp. 350–377, 2016.

[19] C. T. Reid, A. Pillai, and A. R. Black, "The emergence of environmental concerns: Hydroelectric schemes in Scotland," *J. Environ. Law*, vol. 17, no. 3, pp. 361–382, 2005.

[20] A. H. Al-Badi, H. Yousef, O. Alaamri, M. Alabdusalam, Y. Alshidi, and N. Alharthy, "Performance of a stand-alone renewable energy system based on hydrogen energy storage," *ISCCSP 2014 - 2014 6th Int. Symp. Commun. Control Signal Process. Proc.*, no. October, pp. 356–359, 2014.

[21] E. I. Zoulias and N. Lymberopoulos, "Techno-economic analysis of the integration of hydrogen energy technologies in renewable energy-based stand-alone power systems," *Renew. Energy*, vol. 32, no. 4, pp. 680–696, 2007.

[22] X. Tan, Q. Li, and H. Wang, "Advances and trends of energy storage technology in Microgrid," *Int. J. Electr. Power Energy Syst.*, vol. 44, no. 1, pp. 179–191, 2013.

[23] S. Vazquez, S. M. Lukic, E. Galvan, L. G. Franquelo, and J. M. Carrasco, "Energy storage systems for transport and grid applications," *IEEE Trans. Ind. Electron.*, vol.

57, no. 12, pp. 3881–3895, 2010.

[24] Z. Yang *et al.*, “Electrochemical energy storage for green grid,” *Chem. Rev.*, vol. 111, no. 5, pp. 3577–3613, 2011.

[25] B. Hamankiewicz *et al.*, “The effect of electrode thickness on electrochemical performance of LiMn2O4 cathode synthesized by modified sol-gel method,” *Solid State Ionics*, vol. 262, pp. 9–13, 2014.

[26] B. Hu, C. Debruler, Z. Rhodes, and T. L. Liu, “Long-Cycling aqueous organic Redox flow battery (AORFB) toward sustainable and safe energy storage,” *J. Am. Chem. Soc.*, vol. 139, no. 3, pp. 1207–1214, 2017.

[27] T. Nguyen and R. F. Savinell, “Flow batteries,” *Electrochem. Soc. Interface*, vol. 19, no. 3, pp. 54–56, 2010.

[28] P. Alotto, M. Guarnieri, and F. Moro, “Redox flow batteries for the storage of renewable energy: A review,” *Renew. Sustain. Energy Rev.*, vol. 29, pp. 325–335, 2014.

[29] M. Skyllas-Kazacos, M. H. Chakrabarti, S. A. Hajimolana, F. S. Mjalli, and M. Saleem, “Progress in flow battery research and development,” *J. Electrochem. Soc.*, vol. 158, no. 8, pp. 7–10, 2011.

[30] A. Tang, J. McCann, J. Bao, and M. Skyllas-Kazacos, “Investigation of the effect of shunt current on battery efficiency and stack temperature in vanadium redox flow battery,” *J. Power Sources*, vol. 242, pp. 349–356, 2013.

[31] G. Tomazic and M. Skyllas-Kazacos, “Redox Flow Batteries,” *Electrochem. Energy*

Storage Renew. Sources Grid Balanc., pp. 309–336, Jan. 2015.

[32] Q. Huang and Q. Wang, “Next-generation, high-energy-density redox flow batteries,” *Chempluschem*, vol. 80, no. 2, pp. 312–322, 2015.

[33] B. R. Chalamala, T. Soundappan, G. R. Fisher, M. R. Anstey, V. V. Viswanathan, and M. L. Perry, “Redox flow batteries: An engineering perspective,” *Proc. IEEE*, vol. 102, no. 6, 2014.

[34] O. Ijaodola *et al.*, “Evaluating the effect of metal bipolar plate coating on the performance of proton exchange membrane fuel cells,” *Energies*, vol. 11, no. 11, 2018.

[35] K. J. Kim, M. S. Park, Y. J. Kim, J. H. Kim, S. X. Dou, and M. Skyllas-Kazacos, “A technology review of electrodes and reaction mechanisms in vanadium redox flow batteries,” *J. Mater. Chem. A*, vol. 3, no. 33, pp. 16913–16933, 2015.

[36] R. Flückiger, S. A. Freunberger, D. Kramer, A. Wokaun, G. G. Scherer, and F. N. Büchi, “Anisotropic, effective diffusivity of porous gas diffusion layer materials for PEFC,” *Electrochim. Acta*, vol. 54, no. 2, pp. 551–559, 2008.

[37] R. R. Rashapov, J. Unno, and J. T. Gostick, “Characterization of PEMFC Gas Diffusion Layer Porosity,” *J. Electrochem. Soc.*, vol. 162, no. 6, pp. F603–F612, 2015.

[38] V. Gurau, M. J. Bluemle, E. S. De Castro, Y. M. Tsou, T. A. Zawodzinski, and J. A. Mann, “Characterization of transport properties in gas diffusion layers for proton exchange membrane fuel cells. 2. Absolute permeability,” *J. Power Sources*, vol.

165, no. 2, pp. 793–802, 2007.

[39] T. Wang and S. Kumar, “Electrospinning of polyacrylonitrile nanofibers,” *J. Appl. Polym. Sci.*, vol. 102, no. 2, pp. 1023–1029, 2006.

[40] W. Cheng, Q. Yu, Z. Qiu, and Y. Yan, “Effects of different ionic liquids on the electrospinning of a polyacrylonitrile polymer solution,” *J. Appl. Polym. Sci.*, vol. 130, no. 4, pp. 2359–2368, 2013.

[41] R. M. Nezarati, M. B. Eifert, and E. Cosgriff-Hernandez, “Effects of humidity and solution viscosity on electrospun fiber morphology,” *Tissue Eng. - Part C Methods*, vol. 19, no. 10, pp. 810–819, 2013.

[42] J. Doshi and D. H. Reneker, “Electrospinning Process and Applications of Electrospun Fibers,” *J. Electrostat.*, vol. 35, no. 2–3, pp. 151–296, 1995.

[43] D. Wu *et al.*, “Polyethylene terephthalate/poly(vinylidene fluoride) composite separator for Li-ion battery,” *J. Phys. D. Appl. Phys.*, vol. 48, p. 285305, Jul. 2015.

[44] Z. Li and C. Wang, “One-Dimensional nanostructures,” pp. 15–29, 2013.

[45] I. M. Alarifi, W. S. Khan, and R. Asmatulu, “Synthesis of electrospun polyacrylonitrile-derived carbon fibers and comparison of properties with bulk form,” *PLoS One*, vol. 13, no. 8, pp. 1–14, 2018.

[46] L. Mei, R. Han, Y. Fu, and Y. Liu, “Solvent selection for polyacrylonitrile using molecular dynamic simulation and the effect of process parameters of magnetic-field-assisted electrospinning on fiber alignment,” *High Perform. Polym.*, vol. 27, no. 4, pp. 439–448, 2015.

[47] E. Fitzer, W. Frohs, and M. Heine, “Optimization of stabilization and carbonization treatment of PAN fibres and structural characterization of the resulting carbon fibres,” *Carbon N. Y.*, vol. 24, no. 4, pp. 387–395, 1986.

[48] X. Chai *et al.*, “Low-temperature thermal stabilization of polyacrylontrile-based precursor fibers towards efficient preparation of carbon fibers with improved mechanical properties,” *Polymer (Guildf).*, vol. 76, pp. 131–139, 2015.

[49] R. X. Zhao *et al.*, “Influence of heating procedures on the surface structure of stabilized polyacrylonitrile fibers,” *Appl. Surf. Sci.*, vol. 433, pp. 321–328, 2018.

[50] J. H. Kim, H. S. Ganapathy, S. S. Hong, Y. S. Gal, and K. T. Lim, “Preparation of polyacrylonitrile nanofibers as a precursor of carbon nanofibers by supercritical fluid process,” *J. Supercrit. Fluids*, vol. 47, no. 1, pp. 103–107, 2008.

[51] Z. Wangxi, L. Jie, and W. Gang, “Evolution of structure and properties of PAN precursors during their conversion to carbon fibers,” *Carbon N. Y.*, vol. 41, no. 14, pp. 2805–2812, 2003.

[52] K. Yan *et al.*, “Design and preparation of highly structure-controllable mesoporous carbons at the molecular level and their application as electrode materials for supercapacitors,” *J. Mater. Chem. A*, vol. 3, no. 45, pp. 22781–22793, 2015.

[53] Q. S. Ma, A. J. Gao, Y. J. Tong, and Z. G. Zhang, “The densification mechanism of polyacrylonitrile carbon fibers during carbonization,” *Xinxing Tan Cailiao/New Carbon Mater.*, vol. 31, no. 5, pp. 550–554, 2016.

[54] M. Sawawi, T. Yi, D. R. Nisbet, and G. P. Simon, “Scission of electrospun polymer fi

bres by ultrasonication," vol. 54, 2013.

[55] D. C. Marcano *et al.*, "Correction to Improved Synthesis of Graphene Oxide," *ACS Nano*, vol. 12, no. 2, pp. 2078–2078, 2018.

[56] D. R. P. Morris and J. T. Gostick, "Determination of the in-plane components of the electrical conductivity tensor in PEM fuel cell gas diffusion layers," *Electrochim. Acta*, vol. 85, pp. 665–673, 2012.

[57] J. T. Gostick, M. W. Fowler, M. D. Pritzker, M. A. Ioannidis, and L. M. Behra, "In-plane and through-plane gas permeability of carbon fiber electrode backing layers," *J. Power Sources*, vol. 162, no. 1, pp. 228–238, 2006.

[58] S. Mauran, L. Rigaud, and O. Coudevylle, "Application of the carman-kotenzy correlation to a high-porosity and anisotropic consolidated medium: The compressed expanded natural graphite," *Transp. Porous Media*, vol. 43, no. 2, pp. 355–376, 2001.

[59] F. Ambroz, T. J. Macdonald, V. Martis, and I. P. Parkin, "Evaluation of the BET Theory for the Characterization of Meso and Microporous MOFs," *Small Methods*, vol. 2, no. 11, p. 1800173, 2018.

[60] H.-M. Tsai, S.-Y. Yang, C.-C. M. Ma, and X. Xie, "Preparation and Electrochemical Properties of Graphene-Modified Electrodes for All-Vanadium Redox Flow Batteries," *Electroanalysis*, vol. 23, no. 9, pp. 2139–2143, Sep. 2011.

[61] F. Rezaei, R. Yunus, N. A. Ibrahim, and E. S. Mahdi, "Development of short-carbon-fiber-reinforced polypropylene composite for car bonnet," *Polym. - Plast. Technol.*

Eng., vol. 47, no. 4, pp. 351–357, 2008.

[62] H. Ogawa, “Architectural application of carbon fibers development of new carbon fiber reinforced glulam,” *Carbon N. Y.*, vol. 38, no. 2, pp. 211–226, 2000.

[63] H. G. Chae *et al.*, “High strength and high modulus carbon fibers,” *Carbon N. Y.*, vol. 93, pp. 81–87, 2015.

[64] X. Huang, “Fabrication and properties of carbon fibers,” *Materials (Basel).*, vol. 2, no. 4, pp. 2369–2403, 2009.